Chapter 1. Introduction

1.1. Purpose of the work

Recent interest in p-type transparent conductors (TCs) has stimulated research on bulk and thin film properties of materials with hole carriers. Most of the interest is in wide band-gap (above 3.1 eV), high mobility and/or conductivity thin films. The development of transparent p-type semiconductors, along with the already developed n-type materials, should lead to the development of electronic devices such as transparent diodes[1,2], transparent transistors[3], and optoelectronic devices such as light-emitting diodes[4] (LED) and solar cells.

This work is concerned with further broadening of our knowledge on two TC candidates, namely: $CuScO_2$ and $BaCu_2S_2$/$BaCu_2Se_2$.

1.2. Background on transparent conductors

Oxides with the delafossite structure have attracted interest as *p*-type transparent conductors for transparent electrics and electronics applications. The electrical and optical properties of $CuAlO_2$, $CuCrO_2$, $CuGaO_2$ and $CuYO_2$ delafossites were first studied by A.F. Benko and F.P. Koffyburg in the 1980s. Except for $CuAlO_2$, the ceramics were insulating, but Ca doping improved the conductivity of the materials to a measurable level. Primarily they were interested in the optical properties of these materials. For most of them two band gaps were found: a direct and an indirect one. The presence of an indirect gap have never been seen in thin films transmission measurements. Another interesting aspect of their finding was the positive sign of the Seebeck coefficient, which means that the majority carriers in the compound are holes. The results of these original works and of thin films of same materials are summarized in Table 1.1.

Table 1.1. Numerical values of transport and optical properties of previously studied delafossite materials in the bulk and thin film forms.

Material	Conductivity, S/cm	Seebeck coeff, μV/K	Band Gap, eV
Bulk:			
$CuAlO_2$ [5]	1.6_10^{-3}	670	~3.3
$CuCrO_2$:Ca [6]	1.0_10^{-2}	1210	~3.3
$CuGaO_2$:Ca [7]	5.5_10^{-3}	790	~2.7
$CuYO_2$:Ca [8]	2.2_10^{-3}	720	~3.6
Thin Films:			
$CuAlO_2$ [9]	3_10^{-1}	214	3.5
$CuInO_2$:Ca [10]	2.8_10^{-3}	480	3.9
$CuCrO_2$:Mg [11]	220	150	3.1
$CuYO_2$:Ca [12]	1	275	3.5
$CuScO_{2+x}$:Mg [13]	10-20	-	3.3

Transparent thin film conductors with electron type carriers are well studied. Amongst others, In_2O_3:Sn (ITO) with a conductivity of 4000 S/cm, optical transparency of 85% and a band gap of 4 eV [14], with excellent reproducibility in thin film form, is a leader in transparent conducting oxides (TCO). Due to ITO's high transmittance in the visible range and high reflectance in the infrared (IR) range, it is very commonly used as a window coating and solar cells. A very detailed discussion on ITO can be found in Ref 15.

ZnO is a wide direct band gap (3.3 eV) n-type semiconductor due to native defects in the film/powder with electrical conductivity of up to $2 \cdot 10^2$ S/cm [16]. Further enhancement of transport properties can be achieved via Al, Ga, In, Ge doping. In particular aluminum doping this material gives rise to even higher conductivities of 1-$3 \cdot 10^3$ S/cm with optical transmittance of >80% competing with that of ITO [17]. On the other hand it has been proven to be very difficult to dope ZnO p-type because of "hole killer" compensating states forming along with doping of the material. Many theoretical predictions have been made for achieving p-type transport [18,19,20,21], but were not reproducible on experiment [22,23]. Preparation of p-type ZnO is very desirable due to the materials UV light emitting properties [24,25,26]. Successful band gap modulation was obtained by Mg and Cd doping of ZnO, resulting in an increase of the optical forbidden region up to 4 eV and decrease to 3.18 eV [27].

Group III-V nitride based semiconductors have lots of attention and a very precise manufacturing technique have been established for LED's and solid-state lasers [28]. GaN and AlN have appropriate band gaps of 3.4 eV and 6.2 eV, respectively, to be transparent, with low conductivities. These materials were successfully doped n- and p-type with difficult and expensive processing methods, but giving rise to excellent UV LED's. InN with a 1.9 eV low band-gap is a good conductor, and alloys of (Al:In:Ga)N are made to tune the band gap to a particular value for emission at the desired wavelength. These nitride alloys allow for color LED's from UV all the way to yellow. Phosphate based semiconductors (GaP, AlInGaP) and AlGaAs find good application in yellow-green and red LED's, respectively [29]. White light emitting devices are made by pumping a Ce-doped YAG fluorescent layer with blue GaN LED [30]. Experiments with GaAs:N [31] are also being carried out for solar cell applications.

1.3. Organization of the thesis

The general overview on TC's is followed by an introduction to experimental techniques used for data collection presented in the thesis. First the reader will be acquainted with the in line, van der Pauw and rectangular sample four probe conductivity measurements in Chapter 2. It is followed by explanations of Seebeck effect, diffuse reflectance and materials density calculations.

In Chapter 3 the results of a systematic study of magnesium doped and oxygen intercalated $CuScO_2$ materials is presented and discussed. The role of the magnesium doping is very important in unintercalated $CuScO_2$:Mg thin films and pressed powder samples. While in oxygen intercalated thin films the effect of Mg is significantly decreased, in powders there is still a clear dependence on the doping level.

Chapter 4 highlights new results on the effect of potassium doping in $BaCu_2S_2$ and $BaCu_2Se_2$ compounds. These materials are the most conductive p-type compounds we obtained in our labs.

General conclusions, discussion and suggestions for future work are given in Chapter 5.

Chapter 2. Characterization

This chapter describes the equipment and methods of material characterization used throughout this work. This includes the electrical transport measurements conductivity and thermoelectric power (Seebeck coefficient), and absorption and band gap measurements by diffuse reflectance in the uv-visible regime.

2.1. Conductivity measurement

Four-probe direct current (dc) electrical conductivity measurements for sample characterization were carried out using the setup on Fig.2.1. The 4-probe technique is widely used for eliminating contact resistance of the probes. The studied sample is placed on a sample holder (different varieties discussed below) and four probes are attached to surface by means of evaporated or hand-painted metal contacts. A dc current of preset magnitude is supplied to contacts A and D by a Keithley 2400 source, while the voltage drop across B and C probes is measured by a Keithley 195A digital multimeter. The current is supplied in the positive and then negative directions to eliminate any offset voltages that might be present.

For temperature dependent measurements the sample holder is placed on a cold head and inserted into a Pope Scientific cryostat. The bottom of the cryostat is filled with liquid nitrogen at 77K. As the nitrogen evaporates the temperature in the cryostat increases with a 0.5-1 K/min rate to room temperature. A Lakeshore PT-102 platinum resistor is used to monitor the sample temperature; its resistance is measured by a Tektronix DM 5120 programmable digital multimeter. A drawback of the system is that it is open to atmospheric air and the melting ice may cause problems while crossing the 273 K melting point. Such problem was observed during the BaCuSF pressed powder and thin film measurements, in that the conductivity of the samples increased after a temperature dependent measurement. As it turned out, water reacts with BaCuSF resulting in a black mixture compared to the mostly transparent parent material.

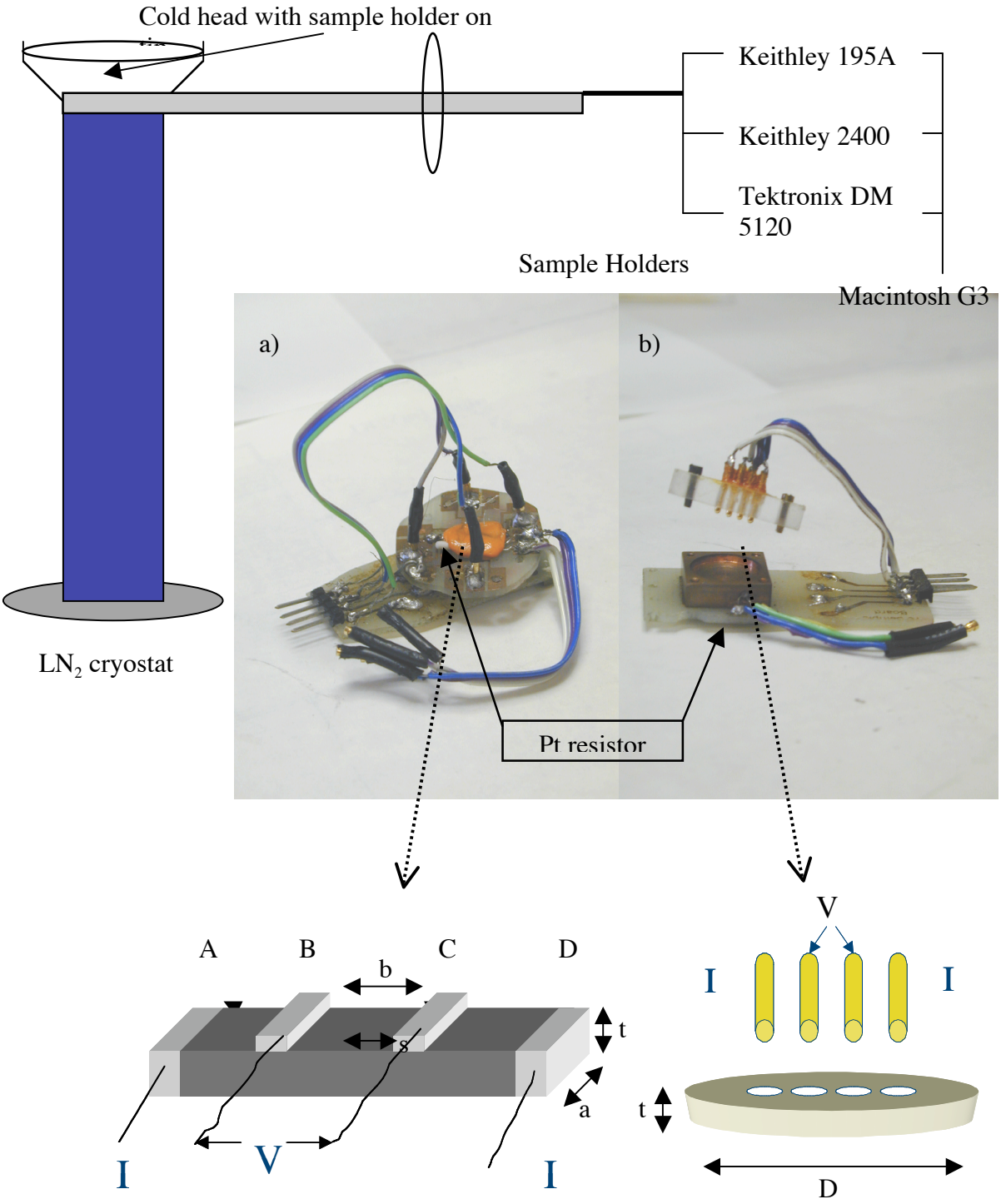

Fig.2.1. Conductivity measurement experimental setup of rectangular (a) and round (b) pellets.

For faster and easier data collection during temperature dependent conductivity measurements, a Macintosh G3 computer connected to the supply and measuring devices via GPIB card automates the setup. A program "KK-R/Tc Measurement" written in Labview v.3 controls the device operation. The program allows one to set the value of the supplied current (between 10^{-2}-10^{-8}A) and read the corresponding voltage, as well as calculate the resistance and the temperature of the measurement. The resistance R calculation is an average of the voltage measurement due to the consecutive positive and negative direction of applied current:

$$R = \left| V_2 - V_1 \right| \Big/ \left| I \right| \tag{2.1}$$

where V_1 is the voltage due to positive current, V_2 is the voltage due to negative current, I is the applied current. The resistance data R' from the platinum resistor, taken before and after each sample resistance measurement loop, is converted to the corresponding temperatures applying the following equation:

$$T=m_1+R'\cdot (m_2+R'\cdot (m_3+R'\cdot m_4)) \tag{2.2}$$

where m_1, m_2, m_3, m_4 are calibration constants. Then the two temperatures are averaged and assigned to the sample resistance.

Since the pressed powder samples come in different shapes (round, rectangular) various sample holders have to be made to accommodate them. In case of rectangular samples, four contacts were hand drawn with silver paint: two on sides and two on top, parallel to each other (Fig.2.1, a). Copper wires (40 gauge) were glued to the pellets by silver paint, soldered to a circuit board and wired to the sourcing and measuring devices. For temperature dependent measurements a platinum resistor was placed under the silly-putty used for holding the sample in place. The current was sourced through the sides, while the voltage drop was measured on the top contacts. The resistivity ρ and conductivity σ of the sample are calculated from the measured resistance (Eq. 2.1) via:

$$\rho = R \cdot a \cdot t / b \tag{2.3}$$

$$\sigma = 1/\rho = b/(R \cdot a \cdot t) \tag{2.4}$$

where a is the short side length of the rectangle, b is the distance between the top contacts, and t is the thickness of the sample.

For round samples I designed a special copper sample holder (Fig.2.1, b), which can accommodate samples with diameter up to 12.7 mm (0.5") and up to 2 mm thick. The measuring probes, 1 mm in diameter and spaced 2 mm apart (center to center), are press fitted in insulating plastic and glued with insulating varnish. A platinum resistor is placed into the copper block under the sample covered with heat conducting paste to monitor the temperature of the sample. Silver contacts were evaporated onto the round pressed powder samples through a mask, also designed by me, in a diffusion-pumped bell jar vacuum system. The current is supplied to outside contacts and the voltage is measured across the two in the middle. The resistance is evaluated by Eq. 2.1, as before. The resistivity/conductivity calculation is not as simple though. For collinear measurements the resistivity is evaluated as [32]:

$$\rho = 2\pi \cdot s \cdot R \cdot F \tag{2.5}$$

where t is the thickness of the sample, s is the probe spacing and F is a correction factor. F is a product of correction factors that depend on sample geometry (thickness, shape, diameter, probe spacing) and type of connection with the sample holder (conducting, insulating). In this work, only insulating substrates are used, and in this case a correction factor F_1, to account for the sample thickness t, is appropriate:

$$F_1 = \frac{t/s}{2 \cdot ln\left(\sinh(t/s) \Big/ \sinh(t/(2s)) \right)} \tag{2.6}$$

In the case of thin films ($t/s < 0.1$) equation (2.5) reduces to:

$$\rho=\pi \cdot R \cdot t/ln(2)=4.532 \cdot t \cdot R \cdot F_2 \tag{2.7}$$

where F_2 depends on the size of the probes relative to the sample diameter, and on their placement. $F_2 = 1$ provided the diameter of the sample is at least 4 times that of the probe spacing. Because the diameter of the samples (D = 12.5 mm) is close to that of the total length of the probes (8 mm), edge effects should be incorporated F_2:

$$F_2 = \frac{ln(2)}{ln(2) + ln\{(\frac{D}{s})^2 + 3\} - ln\{(\frac{D}{s})^2 - 3\}} \tag{2.8}$$

where D is the diameter of the sample, and s is the probe spacing. Typically D = 12.5 mm and s = 2 mm, such that F = 0.818. Other edge effect corrections are in order if a rectangular sample is measured in the inline 4 probe configuration.

The results on samples measured with the above techniques were also subject to verification on a system that uses the van der Pauw method of resistivity measurement. This method also utilizes the advantages of four probes, but any arbitrarily shaped sample can be used. Typically a symmetrical geometry of contacts is used, as shown in Fig.2.2. The contacts are assumed to be negligibly small and located on the sample periphery. In this method, the current is sourced in four possible probe pair configurations and the voltage is measured across the remaining pair of contacts. The resistivity in each configuration is then evaluated by equation (2.7) and the final result is an average of the four measurements. We consider this method to be the reference one to the previously described techniques. Unfortunately, our lab is not equipped to use this method for temperature dependent measurements, unlike the other two methods.

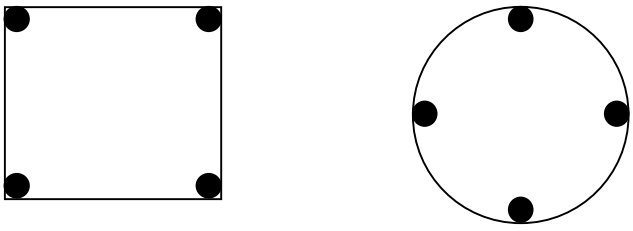

Fig.2.2. Van der Pauw symmetric contact geometries.

Each method gives a very reproducible result for a particular sample (within 5%). On the other hand it is found that the inline method consistently underestimates the resistivity of the measured samples by the inline technique in the range of 10-20% (Fig.2.3), compared to the measurement in the van der Pauw configuration.

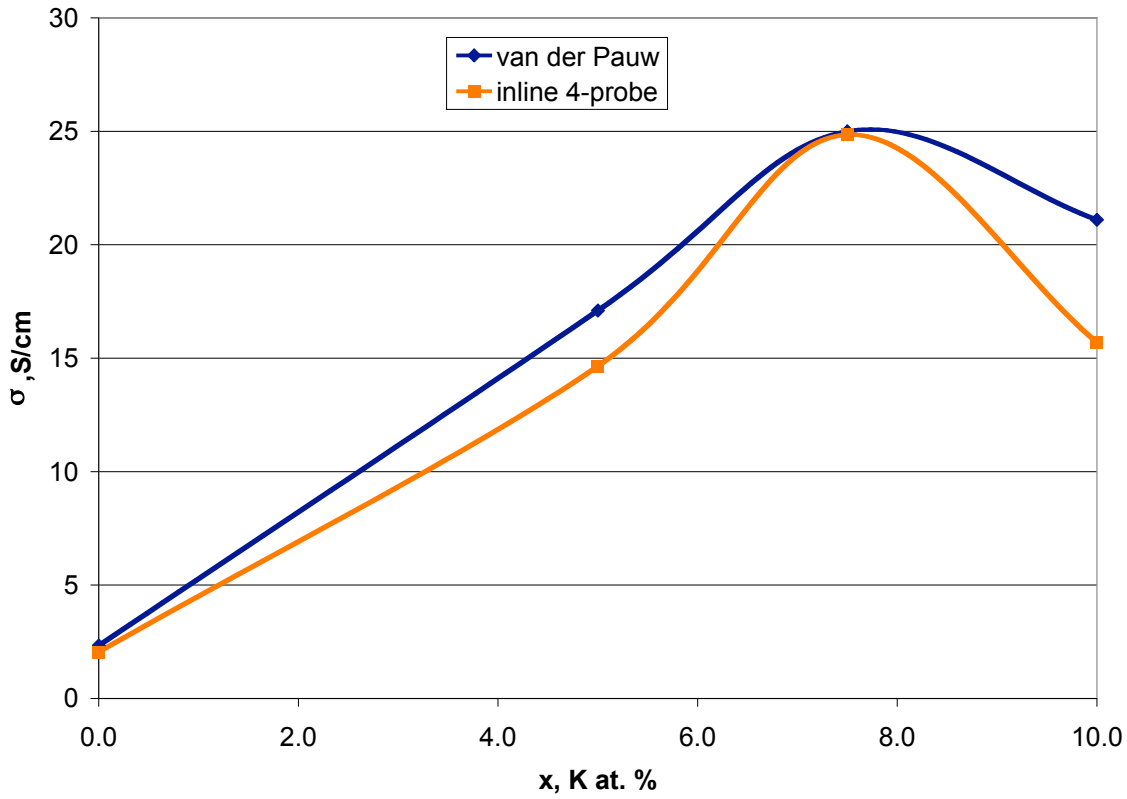

Fig.2.3. The inline technique systematically underestimates the conductivity of the samples. Shown is a set of four $Sr_{1-x}K_xCuSF$ samples with different doping levels.

The Ohmic nature of the contacts established with the surface of the material is determined by current-voltage (*I-V*) measurements. A linear result is an indication of good ohmic contacts. It is generally observed, but as the intrinsic resistivity of the material increases the harder it is to measure, and the *I-V* curve deviates from linear behavior. In case of non-Ohmic contacts, effects like Shottky barriers, strongly affect the measurement results, usually overestimating the resistivity of the samples. In this work

silver contacts were necessary to reproducibly measure the samples with resistivity above 100 Ωcm. Other contact materials should be used for compounds where Ag can cause substitutional doping, which irreversibly changes the sample's characteristics.

The temperature dependent conductivity measurement gives useful information about the carrier transport mechanism. Metals and semiconductors have different temperature dependent transport due to the number of carriers available for conduction and scattering processes involving impurities and phonons. For example, metals exhibit increasing conductivity as the temperature decreases, since a high carrier density is always present, but the electron-phonon scattering process vanishes at low temperatures. In contrast, semiconductors show decreasing conductivity as the temperature decreases. The decrease is often exponential, and may change character in different temperature regimes. The commonly occurring dependences are those of the "thermally activated" and "variable range hopping" (VRH) character. The thermal activation energy is extracted from the slope of the $\ln\sigma$ versus $1000/T$ graph following the law:

$$ó = ó_{max}\, e^{-\frac{E_a}{k_B \cdot T}} \tag{2.9}$$

where σ_{max} is the conductivity at in infinite temperature (all carriers activated), E_a is the thermal activation energy necessary to move a carrier from a localized state (impurity/trap level) to a delocalized one (to the valence band in case of p-type conductors), and k_B is the Boltzman constant. The VRH behavior is governed by the law:

$$ó = ó_{max}\, e^{-(T_0/T)^{1/4}} \tag{2.10}$$

and can be characterized by the temperature parameter T_0, the slope of the $\ln\sigma$ versus $1/T^{1/4}$ [33]. In the VRH scenario the carriers are localized near the Fermi level and the conduction takes place through a combination of carrier hopping between nearest neighbors and tunneling to more distant neighbors whose energies are very similar. The T_0 parameter gives information about the density of states near the Fermi level, but also includes a hopping distance, which the carriers have to overcome for conduction, and can

be also related to a range of energies contributing to hopping. Generally, the lower value of the parameter indicates higher density of states and a higher overlap between them. This leads to improved transport properties, compared to those with higher T_0 values.

2.2. Seebeck coefficient measurement

Measurement of the Seebeck coefficient establishes the carrier type in a material. A positive sign indicates that the conduction mechanism in the material is due to holes (p-type) and a negative sign means due to electrons (n-type). Generally, the magnitude of the coefficient also indicates whether the material is a good (~10μV/K) or poor (>100μV/K) conductor. Together with the electrical σ and heat κ conductivity of the material one can calculate the thermoelectric index of efficiency ZT (or the thermoelectric figure of merit Z) by:

$$ZT = \sigma \cdot S^2 \cdot T/\kappa \qquad (2.11)$$

where S is the Seebeck coefficient and T is the temperature of the measurement. The figure of merit is an important characteristic for thermoelectric cooling (refrigeration) and power generation applications. In thermoelectric coolers, only 30% of the Carnot efficiency could be achieved in materials with ZT = 4. This turns out to be a very challenging task and the highest figure of merit of 3 yet reported can be achieved only in high cost thin films [34].

The principle of the Seebeck effect is the following. Suppose we have a electron type conducting wire, and a voltmeter is connected to its ends reads 0 V, because the two ends are in equilibrium with each other and the environment; no current sources are present. If we now heat one end of the wire (Fig.2.4), a temperature gradient ∇T is established across the wire, and the voltmeter no longer reads 0 V. This phenomenon occurs because while heating one side, the majority carriers in the material gain thermal energy and start to diffuse towards the cold end to bring the system to thermal

equilibrium again. Thus, on the hot side, there is carrier depletion and on the cold side there is a carrier build up, creating an electric field, which opposes the drift of

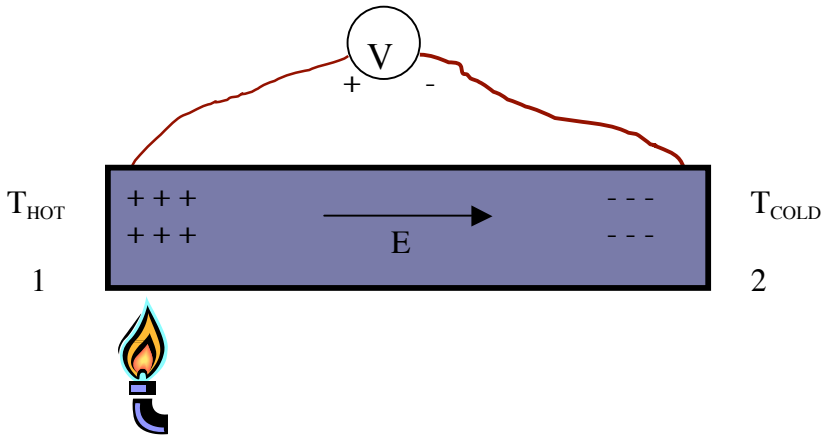

Fig.2.4. Sketch of the Seebeck effect in an n-type material.

electrons towards the cold end. Putting the positive x direction from left to right, one can evaluate the electric field as:

$$E = S\nabla T \tag{2.12}$$

where the Seebeck coefficient (thermoelectric power) S is the proportionality constant. To find the coefficient we need to have measurables in the equation, which are obtained by integrating eq. 2.12 over the length of the wire:

$$\int_1^2 E dx = -\int_{V_{HOT}}^{V_{COLD}} dV = \int_{V_{COLD}}^{V_{HOT}} dV = S\int_1^2 \frac{dT}{dx} dx = S\int_{T_{HOT}}^{T_{COLD}} dT\,, \tag{2.13}$$

where V is the voltage measured across the wire, resulting in:

$$V_{HOT} - V_{COLD} = S(T_{COLD} - T_{HOT}) = -S(T_{HOT} - T_{COLD})\,. \tag{2.14}$$

Let $\Delta T = T_{HOT} - T_{COLD}$ and $\Delta V = V_{HOT} - V_{COLD}$, the Seebeck coefficient is found as:

$$S = -\Delta V / \Delta T . \tag{2.15}$$

Here ΔT is positive by definition, therefore the sign of the Seebeck coefficient is determined by the sign of the voltage measured across the sample (Fig.2.4).

Now, we must take into account the effect of the leads connecting the sample to the voltmeter, which are of a different material. In fact, Fig.2.4 already depicts this situation. In this case the sample and the Cu leads act as a differential thermocouple with unknown Seebeck coefficient of the sample. From the theory of a single junction thermocouple of metals A and B, or double junction differential thermocouples of A-B-A configuration, the voltage measured across the junction(s), connected as on Fig.2.3, is given by [35]:

$$\Delta V = (S_A - S_B)\Delta T . \tag{2.16a}$$

Applying this to the Cu-sample-Cu configuration:

$$\Delta V = (S_{CU} - S_{SAMPLE})\Delta T \tag{2.16b}$$

or

$$S_{CU} - S_{SAMPLE} = \Delta V/\Delta T \tag{2.16c}$$

where ΔV is the voltage across the sample for $\Delta T = T_{HOT} - T_{COLD}$ temperature difference between the Cu leads. Neglecting the Seebeck coefficient of copper ($S_{CU} << S_{SAMPLE}$) we obtain:

$$S_{SAMPLE} = -\Delta V/\Delta T. \tag{2.16d}$$

Therefore, in case the voltmeter on Fig.2.4 returns a negative voltage, the examined material is p-type and vice versa in the case of electrons.

In order to eliminate confusion and provide intuitive result understanding, the polarity of the voltmeter in the experimental setup is switched, such that a measured positive voltage corresponds to hole conducting materials and a negative voltage corresponds to electron conductors.

There are two experimental setups for such measurements available in Dr. Tate's laboratory. One of them accommodates thin films and pressed powder samples of suitable shapes (discussed below) with low temperature measurement capability down to 10 K, built by Till Ulbrich, while the other one can fit pressed powders of common dyes and in principle operates down to liquid nitrogen temperatures, built by Hiroshi Yanagi. I mostly used the system built by Till Ulbrich and will start with its discussion.

The operating principle of the Seebeck coefficient measurement system is simple. The studied sample is pressed between two copper blocks (Fig.2.5). A temperature gradient of 3-4 K is established across the sample by a resistor in one of the blocks, and the corresponding voltage is measured across the sample. The copper block containing the resistor is called the "hot" block, while the other one is the "reference" or "cold" block. The temperature gradient is calculated from the measured voltage across an alumel-chromel-alumel differential thermocouple using the Seebeck coefficient of the thermocouple found from a table published by NIST [36]. The temperature at which the measurement was carried out is monitored by a type K thermocouple installed in the cold block.

For the measurement the resistor (28 Ω) is supplied (typically 5 V) to heat the hot block. When the desired gradient is reached, the resistor is turned off, and the system is allowed to cool down to equilibrium with the surrounding environment. During this time a number of measurement points are taken containing the actual temperature difference of the blocks and a voltage across the sample. Good thermal and electrical contact is necessary between the sample and the blocks for reliable measurements. For rather insulating materials, indium or silver contacts were used.

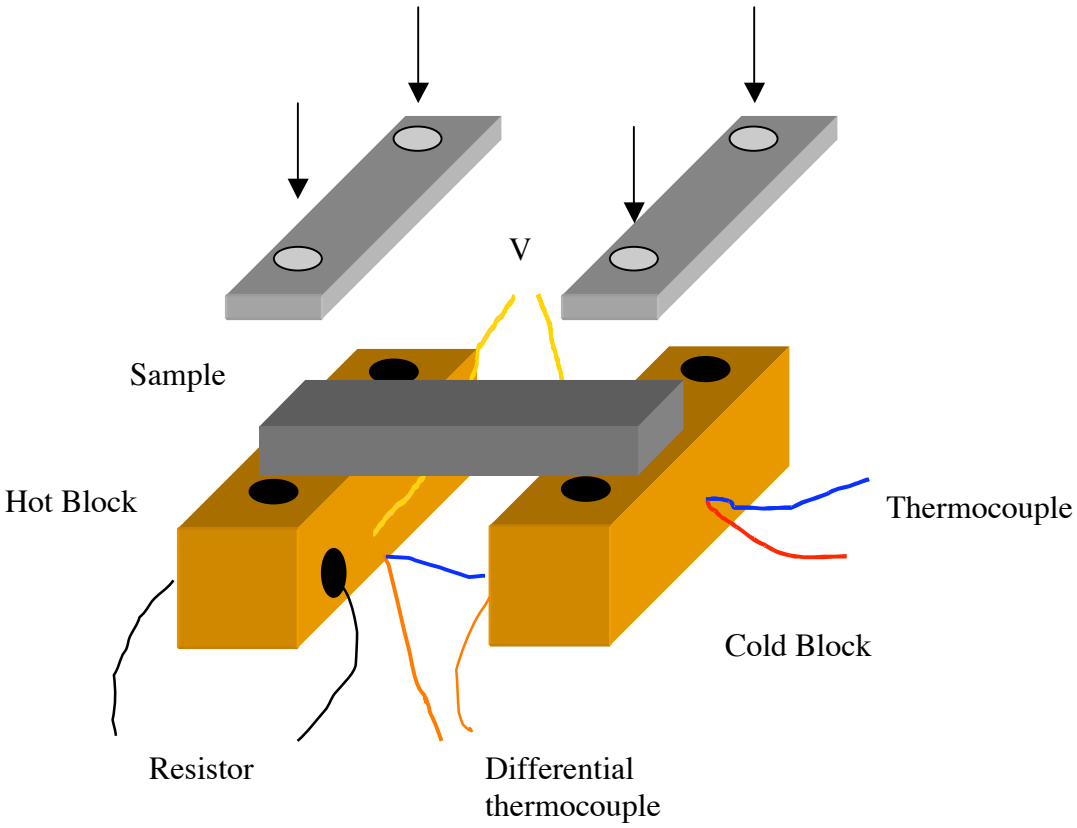

Fig.2.5. Seebeck coefficient measurement: experimental setup.

A typical measurement result is shown in Fig.2.6, where the Seebeck coefficients of chromel and alumel are illustrated and used as a test for the system. The values agree well with the Seebeck coefficient of chromel-alumel thermocouple of S'=40.52 μV/K reported by NIST at 290 K, where $S'=S_{chromel}-S_{alumel}$. [36].

In principle the measured value of the Seebeck coefficient of a material should be corrected by the Seebeck coefficient of the Cu leads. Since this coefficient itself is very low (< 2 μV/K) [37] and the measurement error is consistently about 5 % or less of the measured value (ranging from 40 μV/K to 500 μV/K), the correction would lie well within the experimental error of the device. This was verified by consecutive measurements on the same material. The measured Seebeck coefficient is dependent on the cleanness of the surfaces of the copper contact blocks.

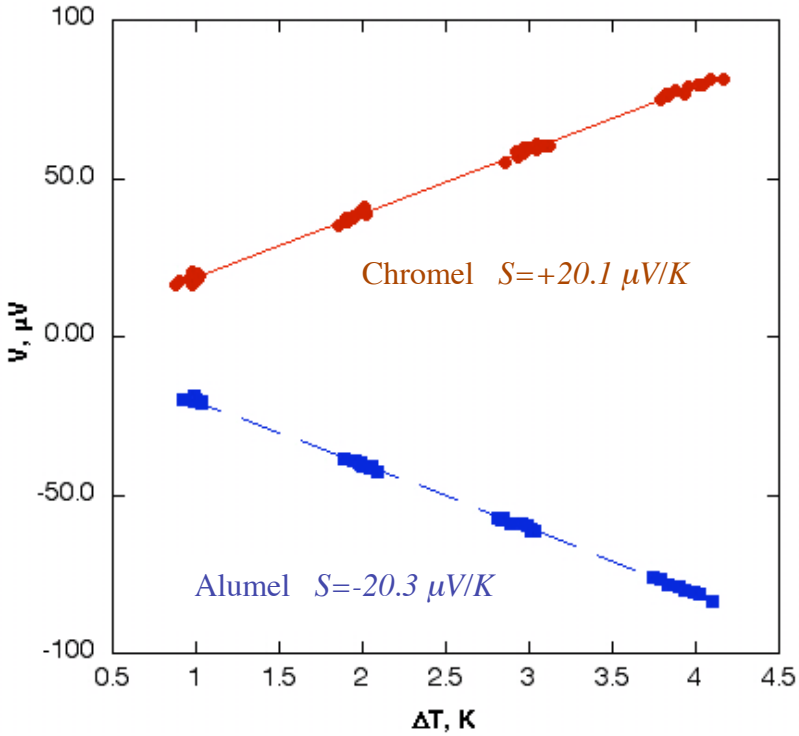

Fig.2.6. The Seebeck coefficient of chromel (red circles) and alumel (blue squares) with a linear fit superimposed. The slopes of the line give the Seebeck coefficient of the materials.

Over time a layer of CuO is formed influencing the electrical and thermal contact to the sample, compromising the measurement results, thus great care is taken to ensure clean contacts.

The above assembly is placed on a cold head in a vacuum chamber for temperature dependent measurements. A thin thermally and electrically insulating plastic is placed between the blocks and the cold head to eliminate fast temperature changes, electrical contact and heat exchange between the blocks. The cold head is in thermal contact with a Leybold closed cycle refrigerator system, using helium as the cooling gas. A low (10^{-5}–10^{-6} Torr) pressure is necessary in the chamber for maximum cooling (minimum heat conduction to the walls of the chamber), established by a Varian portable mini turbopump station. The temperature on the cold head can be adjusted using the

Lakeshore DRC-91CA controller, which refers to the temperature of the cold block, and controls a resistor on the cold head. At temperatures below 50 K the type K thermocouple loses its sensitivity, i.e. gives errors higher than 2% (useful range 70K-1000K). To eliminate this problem, a Si-diode with useful range from 4.2 K to 425 K temperature is attached to the cold head with good thermal contact.

The second device built by Hiroshi Yanagi uses the same principles as above. In this case the pressed powder samples are sandwiched between the copper blocks and placed into a stainless steel crucible. A variety of copper blocks have been made, such that the system can accommodate most pressed powder sample shapes. For temperature dependent measurements liquid nitrogen is poured into the crucible. As the nitrogen evaporates the temperature inside the crucible increases. The drawback of the system is that it cannot be stabilized at a particular temperature for a longer period of time.

This measurement was automated by Dara Easley. She wrote a program called "Seebeck Program" using Labview v.3.0 on the Macintosh G3. The program allows the user to monitor the voltage from the differential thermocouple through the Keithley 195A digital multimeter, the voltage across the sample by the Tektronix DM 5120 programmable digital multimeter, and supplied a voltage up to 4V across the resistor in the "hot" block using the Keithley 2400 source. When the closed cycle refrigerator is running the program also allows setting of the measurement temperature via the Lakeshore controller, ranging from 10 K to 340 K. A more detailed description of the program can be found in Dara Easley's undergraduate honors thesis [35].

The Seebeck effect is less dependent on the grain structure of the studied material, such that it can also give useful information about the transport character. Temperature dependent Seebeck coefficient measurements in particular may give indication about whether a compound is metallic/semimetallic or semiconductor. A metal's or semimetal's temperature dependence can be fitted by:

$$S = S_d + S_p + S_x \tag{2.17}$$

where S_d is a component due to carrier thermal diffusion, S_p is due to phonon drag, and S_x is a term indicating the conduction mechanism. Because the first two are present for

almost all materials, S_x gives more specific information. The thermal diffusion is linearly proportional to T [33], while the phonon drag component is inversely proportional to temperature $\sim 1/T$ [38], therefore the temperature dependence can be fitted by picking two parameters. The third term, for example, can be a contribution from variable range hopping mechanism [39] and is proportional to the square root of the temperature. The total Seebeck coefficient is then found from:

$$S = A \cdot T + B/T + C \cdot \sqrt{T} \ . \tag{2.18}$$

The A, B and C coefficients are related to the density of states near the Fermi surface. In case of materials exhibiting magnetic ordering a magnon drag contribution should be accounted for.

Another possibility to fit the obtained data is to treat the material as a semiconductor, where the mean free path of the carriers can be a defined [39]:

$$S_s = \frac{k_b}{e}\left(\frac{E_C - E_F}{k_b T} + 5/2 + const.\right) \approx D/T + const. \tag{2.19}$$

where k_b is Boltzmann's constant, e the carrier charge, E_C the bottom of the conduction band, and E_F the Fermi level.

2.3. Diffuse reflectance measurement

The optical properties of powder samples were measured by diffuse reflectance method. The light incident on a powder sample is in part transmitted through the crystallites and after multiple reflections escapes the sample, and in part scattered from the grains. Such a measurement gives only qualitative results about the absorption spectrum, because of the indefinite sample thickness and high scattering in the visible and UV regions [40]. Furthermore, the measurement results are influenced by several factors,

such as specular (regular) reflection, moisture and particle size. The specular reflection is common for absorbing materials and can be minimized by dilution of the sample by non- or low-absorbing powders (for example MgO) [41].

A xenon lamp is used as light source in the range of 250-900nm (Fig.2.7). The incident light is separated into a spectrum of wavelengths through a double monochromator, where a 0.25μm grating is used. The resolution is estimated to be around 1 nm. Light of a given wavelength is then guided into an integrating sphere coated with highly reflective $BaSO_4$. The at least 1 mm thick powder sample, contained in a silica crucible of about 10mm in diameter, is placed in the bottom of the integrating sphere, in the path of the incoming beam. The reflected light is gathered by a silicon detector on the equator of the sphere, with an off axis port plug between the sample and the detector, so that only diffusively reflected light is incident on the detector. The intensity of diffusely reflected light as a function of wavelength is recorded. The data collection is automated using HPVee programming and interfacing language written by Derek Tucker and Levi Kilcher [42].

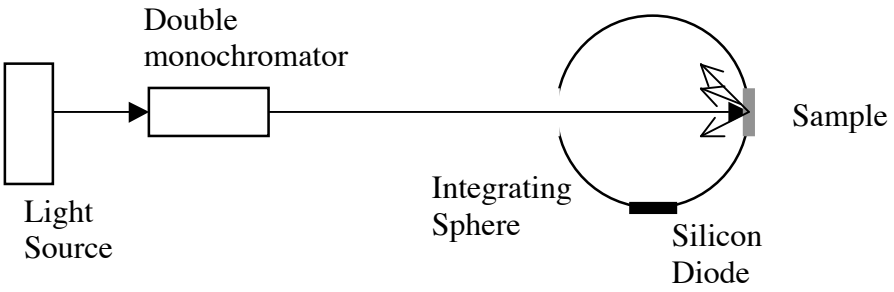

Fig.2.7. Diffuse reflectance measurement.

The gathered data is normalized to the lamp spectrum, obtained using MgO reference powder, that is featureless in the range of interest. The diffuse reflectance is calculated by the Kubelka-Munk method [43,44]:

$$k/s = (1-R)^2/(2 \cdot R) \qquad (2.20)$$

where k is the absorption coefficient, s is the scattering parameter, and R is the normalized reflectance. The absorption coefficient is usually obtained from transmission and reflection of films or crystals, but in powders, diffuse reflection is a reasonable equivalent, since the reflected light has been transmitted through crystallites on the surface of the powder. The measured features of the data are more easily displayed by plotting $E \cdot k/s$ *vs*. E, where E is the energy of the incident light, which is a common practice for determining the direct band gap(s) of the examined material (for example see fig.3.10 in chapter 3.1). First, an absorption onset occurs at high incident photon energies. As the photon energy decreases a maximum in k/s is observed, followed by a sharp drop to almost zero absorption. The band gap is determined from the intersect of a linear fit on the absorption line during the decrease, with the energy axis. The result of such a fit for 3R $CuScO_2$ (fig.3.10) powder yields a 3.3 eV energy band gap.

Chapter 3. Properties of bulk $CuScO_2$:Mg

3.1. Preprint of paper

Structural and transport properties of $CuSc_{1-x}Mg_xO_{2+y}$ delafossites

R. Kykyneshi, B. C. Nielsen, J. Tate*
Department of Physics, Oregon State University, Corvallis, OR 97331
J. Li, A. W. Sleight
Department of Chemistry, Oregon State University, Corvallis, OR 97331

Transport and structural properties of Mg-doped and O-intercalated sintered powders and polycrystalline films of $CuSc_{1-x}Mg_xO_{2+y}$ are reported. Substitution of Mg for Sc systematically increases the *p*-type conductivity in $CuSc_{1-x}Mg_xO_2$ sintered powders, producing a maximum conductivity of 0.015 S/cm at $x \approx 0.06$. A similar level of conductivity is observed in transparent polycrystalline $CuSc_{1-x}Mg_xO_2$ films at the same doping level. Mg doping causes no significant increase in optical absorption at this level. Intercalation of oxygen into the delafossite structure leads to a much larger increase in *p*-type conductivity. In powders, the maximum conductivity is 0.5 S/cm at $y = 0.23$ and $x = 0.05$. In oxygen-intercalated films, the maximum conductivity was 25 S/cm, with the transparent films gradually darkening as oxygen is incorporated. Oxygen intercalation increases the *a*-axis lattice parameter of the delafossite structure in both films and powders, with a much smaller effect on the *c*-axis parameter. Two distinct phases with $y \approx 0$ and $y \approx 0.5$ are observed in x-ray diffraction of powders. In films intermediate values of y are observed, often in combination with a distinct $y = 0$ phase. The absorption properties of the powder samples indicate introduction of defects into the 2H polymorph of $CuScO_2$ and $CuSc_{1-x}Mg_xO_2$ compared to the 3R polymorph.

Key words: transparent conductors, delafossite, p-type conductivity

I. INTRODUCTION

Oxides with the delafossite structure ($CuFeO_2$) have attracted interest as *p*-type transparent conductors. They are also of interest because they exhibit negative thermal expansion [45], they are examples of frustrated magnetic systems [46], and they are also potential thermoelectric materials [47]. Thin films are of particular interest, since it is in this form that applications are most likely to be realized, and there are reports of $CuScO_2$ [13,48], $CuAlO_2$ [9], $CuInO_2$ [10], $CuGaO_2$ [49]. However, investigation of electronic bulk properties is also important because it is easier to control some parameters, like oxygen content [7,8,50].

Delafossites with $A = Cu^+$ in the AMO_2 structure are by far the most studied. These, and similar materials with $A = Ag^+$ are generally semiconductors [51], and are usually transparent when stoichiometric. The *p*-type conductivity of the semiconducting delafossites derives from the introduction of holes into a predominantly Cu-3*d* valence band. Hole doping can be achieved either by the substitution of a divalent species (e.g. Mg^{2+}, Ca^{2+}) onto the octahedral trivalent M-cation site, or by the introduction of excess oxygen, in which case oxygen impurity bands may form [52]. We usually refer to the former process as "doping" or "Mg doping", and to the latter process as "intercalation" or "oxidation". Excess oxygen is located in, or very close to, the planes defined by the triangular arrangement of Cu atoms and in the centers of triangles (see Fig. 3.1). Further details regarding oxygen substitution can be found in an earlier publication [53].

There has been no systematic study of the relative effectiveness of the different types of hole dopants (oxygen *vs*. divalent cation), but it is an interesting question. $CuMO_2$ with M smaller than Sc does not admit excess O, so controllable hole doping for such delafossites can be achieved only by manipulation of the trivalent cation site (and in $CuAlO_2$ and $CuGaO_2$ even this has proven difficult). On the other hand, if M is larger than Sc, oxygen intercalation is allowed and increasingly likely for materials with the largest M cations. The efficacy of each type of dopant is therefore of interest. Hole conduction in $CuMO_2$ appears to be predominantly in the Cu planes (the conductivity is anisotropic [51], and the Cu-3*d* orbitals are the primary contributors to the top of the valence band). Excess oxygen is located in or near the Cu planes [53], and increases the

Cu-Cu distance, thus decreasing the overlap of Cu orbitals and tending to decrease conductivity, but the Cu-O bonds formed may increase the conductivity by providing a direct path. In principle, each excess O provides two holes, but it is not known if they are equally mobile, and it is even possible that one is completely localized. When Mg substitutes on the M cation site, much further from the planes, it is the source of a single hole. Since the M cation orbitals do not contribute to the band structure near the Fermi level, the Cu-O-M-O-Cu linkages are not major contributors to the hole conduction, and any holes produced by Mg substitution at M presumably migrate immediately to the Cu planes.

There are no reports of the effect of cation doping or O intercalation on the transport properties of bulk $CuSc_{1-x}Mg_xO_2$. In previous experiments on $CuSc_{1-x}Mg_xO_2$ films had fixed Mg stoichiometry, and only changes induced by excess O were reported [54]. In the present study, both Mg and O were systematically changed in $CuScO_2$ powders and in films. This proved easier in the bulk form of the material, since processing issues caused Mg depletion in films, as described below. It is recognized that conductivity measurements on sintered powders necessarily reflect a lower bound on conductivity and that processing effects on grain boundaries are very important. We were careful to keep processing conditions as consistent as possible.

II. EXPERIMENTAL DETAILS

Pressed pellets of $CuSc_{1-x}Mg_xO_2$ with $0.01 < x < 0.15$ were prepared from stoichiometric mixtures of CuO (Cerac, 99%), Sc_2O_3 (Stanford Materials, 99.95%), and MgO (Aldrich, 99%). The 12-mm-dia pellets were pressed at 4.5 tonnes producing material with 75% - 85 % of theoretical density. They were placed in a preheated oven, and held in air at 1100˚C for 20 hours, after which they were quenched to room temperature. Mg doping of $CuScO_2$ stabilizes the hexagonal (2H) polymorph of the material, and all the x-ray diffraction patterns could be indexed to this polymorph alone. In addition, pure ($x = 0$) $CuScO_2$ pellets were prepared, in both the 2H and 3R (rhombohedral) forms. To obtain phase pure 3R $CuScO_2$, a small (about 1%) Sc excess was used, and the pellet was heated in air at 600˚C/h to 1100˚C, held for 24 h and

quenched. The phase pure 2H form was obtained by the same process as the Mg-doped samples, except that no MgO was used, but rather a small Cu excess.

Oxygen intercalation of pure 2H and 3R $CuScO_2$ and of Mg-doped $CuSc_{1-x}Mg_xO_2$ was achieved under $9\cdot 10^4$ torr of oxygen at 420˚C for 6 days in a quartz tube. The intercalation was prohibitively slow in sintered material, but possible in powder or cold-pressed material, so the sintered pellets were reground, cold-pressed into bar form, and oxygen treated.

Films were prepared by rf sputtering from targets of $CuScO_2$, $CuSc_{0.95}Mg_{0.05}O_2$, and $CuSc_{0.85}Mg_{0.15}O_2$ in an Ar/O_2 (100:1.5) mixture at 12 mtorr. The substrate was pure amorphous SiO_2, held at temperatures between 150˚C and 350˚C. The deposition rate was about 0.02 nm/s and films were typically 150 nm thick. Following deposition, the brownish-tinted films were subjected to a 15-minute rapid thermal anneal (RTA) cycle first in oxygen at 750˚C and then in argon at 900˚C. This process produces transparent, polycrystalline $CuSc_{1-x}Mg_xO_2$ films with only the slightest hint of color. Electron probe microanalysis reveals that the Mg content of the target is reproduced in the as-deposited films, but only approximately one third of the Mg remains after the RTA process. Presumably the maximum Mg incorporated in films was 5% (i.e. $CuSc_{0.95}Mg_{0.05}O_2$) from the target with 15% Mg, but the fate of the rest of the Mg is not established. For consistency, films are referred to by the Mg content of the target from which they were prepared. Oxygen was intercalated by placing the films in a quartz tube furnace in 400 torr of O_2 at 400˚C for 9 h. In some cases, a high pressure intercalation process was conducted in a stainless steel tube furnace at $5\cdot 10^4$ torr and 400˚C for 24 h.

In what follows, measurements are reported for samples with the same Mg content but different oxygen content. In the case of bulk material, two sintered pellets were produced under identical conditions from the same starting powder, ensuring identical Mg content, and one of the pellets was reground, cold pressed, and oxidized. In the case of films, a single sputtered film was cleaved into two smaller films that underwent identical treatment until the intercalation step.

The structure of the bulk material was examined by X-ray powder diffraction on a Siemens D5000 diffractometer with Cu $K\alpha$ radiation. The oxygen content was analyzed

by thermogravimetric analysis (TGA). Film structure was determined using a Rigaku Rapid diffractometer with the incident beam at grazing incidence and a curved image plate detector. The increase in oxygen content of the films was qualitatively established by electron microprobe measurements, and the increase of the lattice parameter upon oxygen intercalation and the darkening of the films confirm that oxygen uptake occurs.

Temperature-dependent conductivity measurements of pellets and films were conducted in a liquid nitrogen cryostat in the 120 – 290 K temperature range. Silver contacts were used to minimize contact resistance and a 4-probe co-linear geometry was used for the unoxidized circular pellets. Silver contacts and a 4-probe technique appropriate to bar geometry were used for the oxidized samples. Several circular pellets of unoxidized material were modified to bar shape and their conductivities remeasured in the new geometry. Conductivities were reproducible within about 10%. The carrier type was determined by measurements of the Seebeck coefficient at room temperature. A temperature gradient of about 3 K was established across the sample, and the resulting thermoelectric voltage was measured.

Diffuse reflectance spectra of powdered samples between 250 nm and 900 nm were obtained using a Xe lamp and a grating double monochromator as the source, and collecting light diffusely reflected by the powders with an integrating sphere and detecting it with a Si diode detector. These data were normalized to the signal obtained from MgO powder under the same conditions. The same source was used to measure reflection and transmission of the thin-film samples. In this case, no integrating sphere was necessary, since diffuse scattering is small.

III. RESULTS AND DISCUSSION

A. Structural properties

The $CuSc_{1-x}Mg_xO_2$ pellets (prior to oxygen intercalation) exhibited powder x-ray diffraction patterns that could be completely indexed to the 3R or 2H polymorphs of $CuScO_2$ [55]. The pellets were phase pure up to 5% Mg doping; at larger concentrations, small amounts of MgO and Cu_2O were present. This indicates a limited solubility of Mg in $CuScO_2$. The Mg^{2+} ionic radius (0.72 Å) is about 3% smaller than that of Sc^{3+} in the same coordination (0.745 Å) [56]. The Mg doping results in a small decrease (–0.04%)

of the *a*-lattice parameter in powders up to 5% Mg doping, while the *c*-lattice parameter changes even less. The 3R polymorph was obtained when no Mg was incorporated and a slight Sc excess was present. The 2H polymorph resulted for the Mg-doped samples and for the sample containing no Mg and a slight Cu excess, provided the powder was prepared in a preheated oven (slow heating always results in some 3R phase). The structural similarities between the Mg-doped material and the "Cu-doped" material suggest that the Cu excess necessary to stabilize the 2H form of $CuScO_2$ enters as Cu^{2+} on the Sc^{3+} site. The Cu^{2+} ion (0.73 Å) is an even closer match to the Sc^{3+} ion size, so this substitution is highly likely. Moreover substitution of Cu^{2+} on an octahedral site is known to occur, for example in $Cu_2(CuTi)O_4$ [57].

After oxidation of the pellets, the x-ray diffraction pattern exhibits interesting structure as shown in Fig. 3.2, where the pattern of intercalated 2H $CuSc_{0.95}Mg_{0.05}O_{2+y}$ is shown together with the pattern for unoxidized 2H $CuSc_{0.95}Mg_{0.05}O_2$. It is evident that each peak splits into two, and that one of the members of the split pair is closely aligned with the corresponding reflection in the unintercalated sample, while the other is shifted to smaller 2θ. The change is most striking for the (110) reflection near 2θ = 57.3˚, with a shift of 0.8˚. It is much smaller for the (00*l*) reflections [53], and in this particular set, the data for the oxidized material include a small offset of 0.15˚ to bring the (004) reflections near 2θ = 31.6˚ into alignment. The powder x-ray diffraction patterns indicate that the oxygenated powder is really an intimate mixture of two distinct compositions. More detailed studies [53] have shown that these compositions are very close to $CuScO_2$ and $CuScO_{2.5}$. (Note that here, $CuScO_{2.5}$ is the delafossite structure, which is either hexagonal or rhombohedral, with excess O in the Cu planes, and not $Cu_2Sc_2O_5$ which is orthorhombic and belongs to a different space group.) The extra oxygen entering the 2H lattice takes up interstitial sites in or close to the Cu-plane and expands the *a* lattice parameter by about 1.5%. TGA of such samples revealed an average oxygen content between 2 and 2.5 per formula unit, as expected.

Examples of the x-ray diffraction patterns of $CuSc_{0.99}Mg_{0.01}O_{2+y}$ films with $y \approx 0$ and $y \approx 0.5$ are presented in Fig. 3.3. The large shift of the (110) reflection is again evident, showing the increase in the *a* lattice parameter, and a very small effect on the (00*l*)

reflections and hence on the *c* axis parameter. The film reflections index to the 3R reflections, but some 2H component is present. The (*hk0*) and (*00l*) reflections are almost exactly coincident for 3R and 2H, and are therefore insensitive to stacking faults, which is why they are the narrowest and most symmetric peaks. Details of the thermal processing affect the formation of the different polytypes, and we are unable to control this well enough in films to produce a phase-pure polytype. There is a recent report of 3R epitaxial films of $CuScO_2$ by PLD on crystalline Al_2O_3 [48]. Although the oxygen content could not be directly determined in our films, the value of the *a*-axis lattice parameter is a good indicator. We usually determined this from the position of the (110) reflection, but a refinement of the spectrum was performed for several films, and the agreement is good. The powder data, extensively refined, give reference points for $y = 0$ and $y = 0.5$. In many films, we also observe the simultaneous presence of an unoxidized phase ($y \approx 0$) with an oxidized phase. In films, the *a*-axis lattice parameter of the oxidized phase is consistent with values *other* than $y = 0.5$, unlike in powders where only $y = 0.5$ is observed for the oxidized portion. This difference is attributed to non-equilibrium conditions in the films, probably strain and other defects. Fig. 3.4 shows the measured *a* lattice parameter for films as a function of oxygen intercalation pressure. The different symbols indicate different sets of films, which differ in Mg content, but as noted previously Mg incorporation has a negligible effect on the *a* axis lattice parameter. The films intercalated at 400 torr (solid square) and at 50,000 torr (open triangle) are examples where two phases, one unoxidized and the other oxidized or partially oxidized, were identified by a clear splitting of the (110) reflection. It is worth noting that films made by pulsed laser deposition (open triangle) were significantly more difficult to oxidize. These films were *c*-axis oriented in contrast to the polycrystalline sputtered films, and the slow oxidation characteristic of the bulk is also displayed here.

One other structural point is worth mentioning. Our procedure involves an oxidation step that results in the orthorhombic $Cu_2Sc_2O_5$ phase [58]. These films are polycrystalline and have a greenish hue. The subsequent reduction in Ar produces $CuScO_2$, which is almost colorless, but sometimes has a slight pink hue. There is no intrinsic reason why the production of $CuScO_2$ should proceed via the $Cu_2Sc_2O_5$ phase,

and indeed we have produced films of $CuScO_2$ without this step, but it seems to be more reliable and reproducible to first oxidize the copper completely [59].

B. Transport properties

The room temperature conductivity as a function of Mg doping for the unoxidized $CuSc_{1-x}Mg_xO_2$ pellets is shown in Fig. 3.5, along with the Seebeck coefficient for the same samples. There is an approximately linear improvement in conductivity with increasing Mg content up to around $x = 0.06$ where it reaches $1.5 \cdot 10^2$ S/cm. Further increase in the Mg content decreases the conductivity. This suggests that Mg^{2+} enters substitutionally until at least $x = 0.06$. Note that the conductivity of the "undoped" 2H $CuScO_2$ is comparable to the Mg-doped samples for small values of x. This supports the conjecture that the excess Cu necessary to stabilize the 2H phase enters as Cu^{2+} on the Sc^{3+} site and contributes a hole. The conductivities are more than an order of magnitude higher than for the 3R phase of $CuScO_2$. If one assumes that the conductivity can be written $\sigma = pe\mu$, where p is the number density of holes introduced by the Mg substitution and e the magnitude of the electronic charge, the data below $x = 0.06$ can be reasonably well represented by a "mobility parameter" $\mu = 5.8 \cdot 10^{-5}$ cm^2/Vs. This is not a true mobility but a parameter that incorporates ionization efficiency as well as intrinsic mobility, but the low value is certainly consistent with the difficulty in measuring a Hall mobility in either powders or films, and indicates that the doping efficiency and the mobility are probably both small.

The Seebeck coefficients of all the samples are positive, indicating p-type conductivity. The values (400 – 500 μV/K) are typical of poor conductors, but more important is that the trends in the Seebeck coefficient mirror the conductivity measurement trends, with higher values for the less conductive samples and lower for more conductive ones. Since the Seebeck effect is less dependent on grain structure or sample geometry than conductivity, this indicates that the conductivity is probably not determined entirely by grain structure but rather reflects the Mg content. This is further supported by thin film results where the conductivity of $CuSc_{1-x}Mg_xO_2$ is about the same order of magnitude as for powders in the same x range. Temperature-dependent

conductivity measurements were also performed and reflect predominantly variable range hopping (VRH) character especially below 200 K. VRH behavior follows the law

$$\sigma = \sigma_\infty e^{-(T_0/T)^{1/4}}$$

and can be characterized by the temperature parameter T_0, the slope of the graph of lnσ versus $T^{1/4}$. This parameter is presented in Table 3.1, along with the sample densities.

We now turn to the results for the set of oxidized (intercalated) $CuSc_{1-x}Mg_xO_{2+y}$ pellets. The room temperature conductivities and Seebeck coefficients as a function of Mg content x, are displayed in Fig. 3.6. The overall behavior is superficially similar to the unoxidized samples with a broad maximum near $x \approx 0.05$. The conductivities are larger by about 1.5 orders of magnitude over those of the corresponding unoxidized pellets, with a maximum value of about 0.5 S/cm. Once again the Seebeck coefficient trend mirrors the conductivity trend, and the overall values are smaller by about a factor of 3-4, as expected for more conductive material. The improved conductivity is, of course, induced by the oxygen excess, which was measured by TGA for each sample, and Fig. 3.7 illustrates that the conductivity correlates with the oxygen excess. Fig. 3.8 displays the conductivity, corrected by subtracting the small value for the corresponding unoxidized material, as a function of oxygen excess y. Again assuming the validity of $\sigma = pe\mu$, we calculate the number density on the premise of two holes per oxygen, and find that a "mobility parameter" of about $3.6 \cdot 10^{-4}$ cm^2/Vs fits all the data reasonably well - there is also no saturation effect. As before, one should be circumspect about the interpretation of this parameter, but it is about a factor of 6 higher than the parameter found for the unoxidized materials. The difference in "mobility parameter" is significant but not extremely large. Thus the large conductivity of oxidized $CuSc_{1-x}Mg_xO_{2+y}$ can be mostly accounted for by the fact that $CuScO_2$ accommodates more excess oxygen than substituted Mg. Excess oxygen can be intercalated up to 0.5 per formula unit (1 hole per formula unit if both holes contribute to the conductivity), whereas Mg can be substituted only at the level of about 0.05 holes per formula unit before adversely affecting conductivity.

The oxygen excess represented in Fig. 3.8 is an average value for each sample – we have noted previously that the $CuSc_{1-x}Mg_xO_{2+y}$ powders are mixtures of phases with compositions close to $CuSc_{1-x}Mg_xO_2$ and $CuSc_{1-x}Mg_xO_{2.5}$. The intercalation of oxygen is very slow, so it is likely that each grain consists of an oxidized shell surrounding an unoxidized center.

It is not entirely clear why the oxygen uptake depends on the Mg doping at all, and why it peaks near the Mg solubility limit. Mg doping slightly *decreases* the $CuScO_2$ lattice parameter, so increased Mg content should inhibit oxygen uptake, not enhance it. It is in principle possible that the crystallite sizes were different for different Mg content, and this influenced the oxygen uptake. In favor of this argument is that all Mg doped material was identified as the 2H polymorph, and this phase routinely has larger crystallite sizes and is more difficult to oxidize. Thus small variations in size could produce significant variations in average oxygen uptake. On the other hand, x-ray spectra provide no evidence for significant crystallite size variation. Whatever the reason for the observed larger oxygen uptake near $x \approx 0.5$, it raises an important question: could the "unoxidized" materials with similar x value have taken up a small amount of oxygen during synthesis (for example during the quench from 1100˚C), so that their conductivity is really oxygen induced rather than Mg induced? The answer appears to be "no" for several reasons. First, neither TGA nor x-ray diffraction of the unoxidized $CuSc_{1-x}Mg_xO_2$ materials gives any indication of excess oxygen. Second, the oxidized materials were ground one additional time compared to their unoxidized counterparts, so crystallite size variations should be different. Finally, thin film conductivity results, discussed below, also show that the addition of Mg improves conductivity.

The oxidized 3R and 2H phases of bulk $CuScO_{2+y}$ (no Mg) also show improved transport properties over their unoxidized counterparts. The 2H $CuScO_2$ is again of comparable conductivity to the Mg-doped powders. In the case of the 3R $CuScO_2$, the improvement in conductivity upon oxidation is very large ($7 \cdot 10^{-4}$ S/cm to 0.2 S/cm upon oxidation). This may result from improved oxygen incorporation arising from the generally smaller grain sizes in 3R powder [53]. The conductivity of all the oxidized materials is less temperature dependent than for the corresponding unoxidized materials, which results in lower values of the parameter T_0, as shown in Table 3.2. It is also not

possible to fit all the data with a single VRH form, so the values in Table 3.2 are for temperatures below 160 K.

The conductivity for $CuSc_{1-x}Mg_xO_{2+y}$ films as a function of Mg content in the sputter target is shown in Fig. 3.9. Unoxidized films with no Mg doping ($y = 0$, $x = 0$) have very low conductivities ($<10^{-4}$ S/cm), and the incorporation of Mg increases the conductivity by about two orders of magnitude to the level of 10^{-2} S/cm (similar to powders). The conductivity of the film with higher Mg content ($x = 0.15$ in sputter target) is slightly smaller than that of the film with $x = 0.05$ in the sputter target. Although there are only two doping levels, the results are consistent for several preparation conditions (including more than the two shown here). The overall increase of the conductivity upon uptake of oxygen is a further two orders of magnitude to a level of 1-5 S/cm for the films intercalated at 400 torr. In this case the conductivity continues to increase with increasing Mg doping. Upon high pressure oxygen intercalation ($5 \cdot 10^4$ torr), the conductivity reached about 25 S/cm for undoped and Mg doped films. We have no quantitative measure of the oxygen content of the films, but films intercalated with oxygen at 400 torr were all intercalated simultaneously, so the oxygen uptake should be the same. The increased conductivity for higher Mg doping in this case could be the result of a co-doping effect where the presence of the oxygen improves the efficiency of hole generation by the Mg, or improves their mobility by providing increased orbital overlap in the Cu planes (or Cu-O planes in this case). However, this would have to be investigated more carefully for several levels of Mg doping, and would require quantitative oxygen analysis. In the heavily intercalated films, the conductivity is high enough that the dependence on Mg concentration is no longer evident. The maximum conductivity achieved in intercalated films is 10 – 50 times higher than in powders. Since the conductivity for the unoxidized films and powders is similar, the lower conductivity in powders is unlikely to be due to grain boundary effects, but rather to incomplete oxidation of the powdered materials.

C. Optical properties

The results of the diffuse reflectance measurements of the unoxidized 3R and 2H $CuScO_2$ powders and of unoxidized $CuSc_{1-x}Mg_xO_2$ powders for x = 0.02 and 0.04 are graphed in Fig. 3.10. The diffuse reflectance (relative to MgO), $R(\lambda)$, was recorded as a function of wavelength. The ratio $(1-R)^2/2R$ gives the ratio of the absorption coefficient to the scattering factor at that particular wavelength. To the extent that scattering is not expected to vary considerably over the wavelength of interest, this ratio may be considered proportional to the absorption coefficient, usually called α. The absorption coefficient can be obtained directly from true transmission and reflection measurements on thin films or crystals, but for powders, diffuse reflection is considered a reasonable equivalent. (Diffusely "reflected" light from loose powders has in fact also been transmitted through tiny crystallites near the surface.) It is common practice to plot $(\alpha E)^2$ versus E (where $E = hc/\lambda$ is the photon energy) and determine a direct band gap from the intercept of the plot with the $(\alpha E)^2 = 0$ axis. Such a representation is found in Fig. 3.10. The values for the band gap thus determined from diffuse reflectance may not be entirely accurate given the approximations, but they should clearly indicate trends.

The 3R $CuScO_2$ is very slightly gray in color and its diffuse reflectance spectrum is very clean and allows an unambiguous band gap to be identified. It was estimated at about 3.3 eV and is qualitatively in agreement with values measured in thin films [54,48]. The "undoped" 2H phase $CuScO_2$ powder is a darker gray as is to be expected from the overall higher absorption in the visible region. There is also an additional feature in diffuse reflectance near 3.3 eV. However, the spectrum looks very similar to that of the 3R material above about 3.4 eV, and it would be difficult to argue that the band gap has been decreased. Rather, it appears that the incorporation of excess Cu^{2+} introduces states in the gap that contribute to absorption. Incorporation of Mg^{2+} into the samples further darkens the material as is evidenced by increased absorption near 2.3 eV for both the x = 0.02 and x = 0.04 powders. The oxidation process converted all the $CuScO_2$ and $CuSc_{1-x}Mg_xO_2$ samples to black powders that were too absorbent to produce meaningful diffuse reflectance spectra.

Reflection and transmission spectra of films confirm the visual impression that $CuScO_2$ films are transparent in the visible region, and are not rendered more absorbing by the incorporation of Mg at the levels investigated here. These films have a direct band gap of 3.6 eV. Intercalation of oxygen causes increased absorption across the visible spectrum. The highly conductive films darken, but retain transmission around 70% for wavelengths longer than 700 nm. At 550 nm, transmission is about 50%, and decreases for shorter wavelengths.

IV. SUMMARY

Changes in structural and transport properties of $CuScO_2$ powders and films upon substitution of Mg for Sc and intercalation of oxygen are reported. Mg doping and oxygen intercalation both increase *p*-type conductivity in $CuScO_2$, and the conductivity can be varied by 5 orders of magnitude with various combinations of dopants. The effectiveness of each type doping appears to be similar, and the larger conductivity resulting from oxygen intercalation is most simply explained by the capacity of the structure to incorporate a large oxygen excess (up to $y = 0.5$ in $CuSc_{1-x}Mg_xO_{2+y}$) with continued increase in conductivity, whereas its ability to substitute Mg is limited to $x < 0.06$.

Oxygen intercalation expands the $CuScO_2$ lattice, mainly by increasing the *a*-axis lattice parameter. X-ray diffraction indicates that the oxidized bulk material consists of a mixture of two phases with compositions close to $CuSc_{1-x}Mg_xO_{2.0}$ and $CuSc_{1-x}Mg_xO_{2.5}$. In films, such mixtures are also observed, but the oxygen content of the oxidized phase may be less than 2.5.

The increased conductivity $CuSc_{1-x}Mg_xO_{2+y}$ has a significant effect on the optical absorption of the material. Diffuse reflectivity of powders indicates that the 3R polymorph is virtually defect free, with little absorption of light at energies below 3.4 eV. The 2H polymorph stabilized by excess Cu shows increased absorption across the visible spectrum, as do the 2H polymorphs stabilized by Mg substitution, which also have additional absorption at 2.3 eV. Films of $CuSc_{1-x}Mg_xO_2$ are highly transparent, even with Mg substituted at the level of several percent, but show increased absorption over the visible range upon oxygen intercalation.

ACKNOWLEDGEMENTS

We thank A. Draeseke for early contributions to the thin film preparation, Dr. R. Nagarajan for preliminary x-ray data analysis, Prof. W. W. Warren for numerous useful discussions, and Dr. A. Yokochi for x-ray diffraction of thin films. This work is partially supported by the National Science Foundation (DMR 007127 and DMR 02445386), by the Army Research Office (E-18-667-G3) and by the Research Corporation.

References:

* Corresponding author, tate@physics.orst.edu

TABLES:

Table 3.1. Density (% of theoretical) and VRH parameter T_0 ($160 < T < 290$ K) from temperature-dependent conductivity measurements of unoxidized $CuSc_{1-x}Mg_xO_2$ pellets.

Mg doping, *x*	Density, %	$T_0^{1/4}$ ($K^{1/4}$)
0.01	76	180
0.02	76	168
0.03	80	161
0.04	83	163
0.05	83	163
0.06	81	163
0.07	85	153
0.09	85	153
0.10	83	153
0.12	85	139
0.15	83	150

Table 3.2. Density (% of theoretical) and VRH parameter T_0 ($T < 160$K) from temperature-dependent conductivity measurements of oxidized $CuSc_{1-x}Mg_xO_{2+y}$ pellets.

Mg doping, *x*	Density, %	$T_0^{1/4}$ ($K^{1/4}$)
0.01	75	57
0.02	76	56
0.03	71	68
0.04	75	68
0.05	71	77
0.06	79	71
0.07	73	67
0.09	79	64

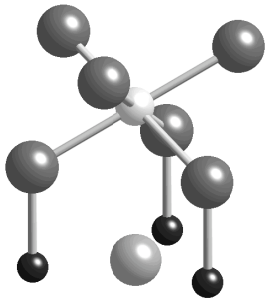

FIG. 3.1. Part of the AMO_2 delafossite structure showing the site of the O dopant. Small dark spheres are Cu atoms forming a triangle around the interstitial oxygen atom. The light sphere is a Sc atom (for which Mg substitutes) bonded to 6 oxygen atoms. In the 3R form, the interstitial oxygen atom is displaced by about 0.3 Å out of the Cu plane toward the Sc atom.

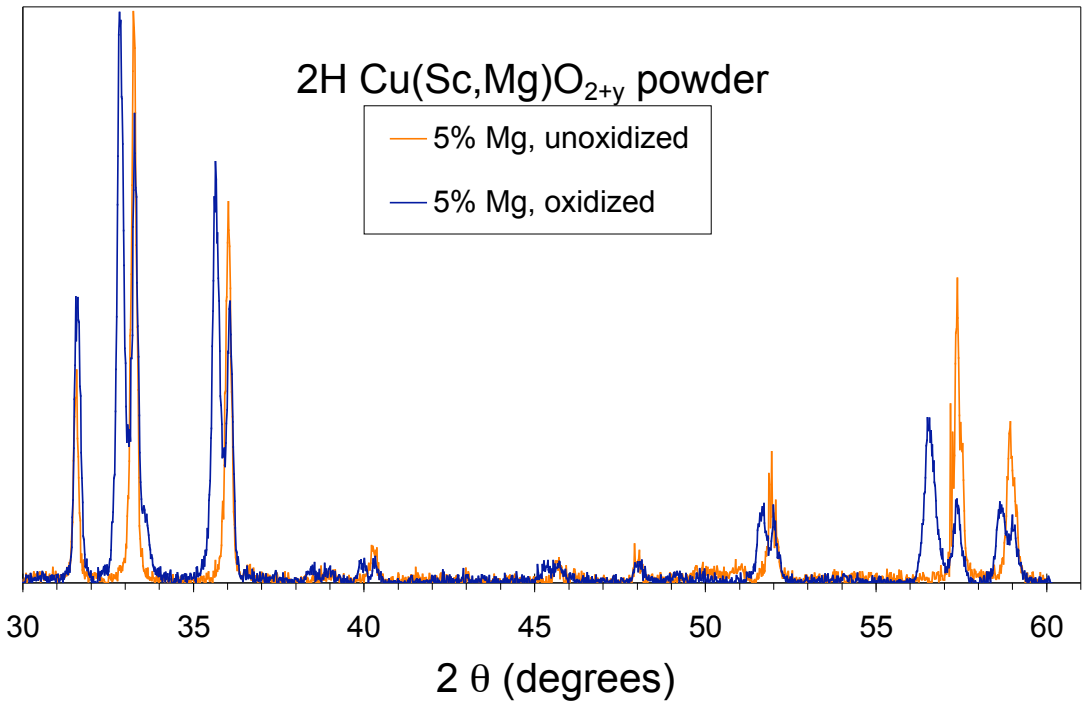

FIG. 3.2. (Color online) X-ray diffraction patterns of unoxidized (light/orange line) $CuSc_{0.95}Mg_{0.05}O_2$ and oxidized (dark/blue line) $CuSc_{0.95}Mg_{0.05}O_{2+y}$ bulk powders. Two features are prominent: the splitting of the peaks in the oxygen-intercalated sample and the shift of one of the split pair to smaller 2θ. The shift is largest for (*hk0*) reflections.

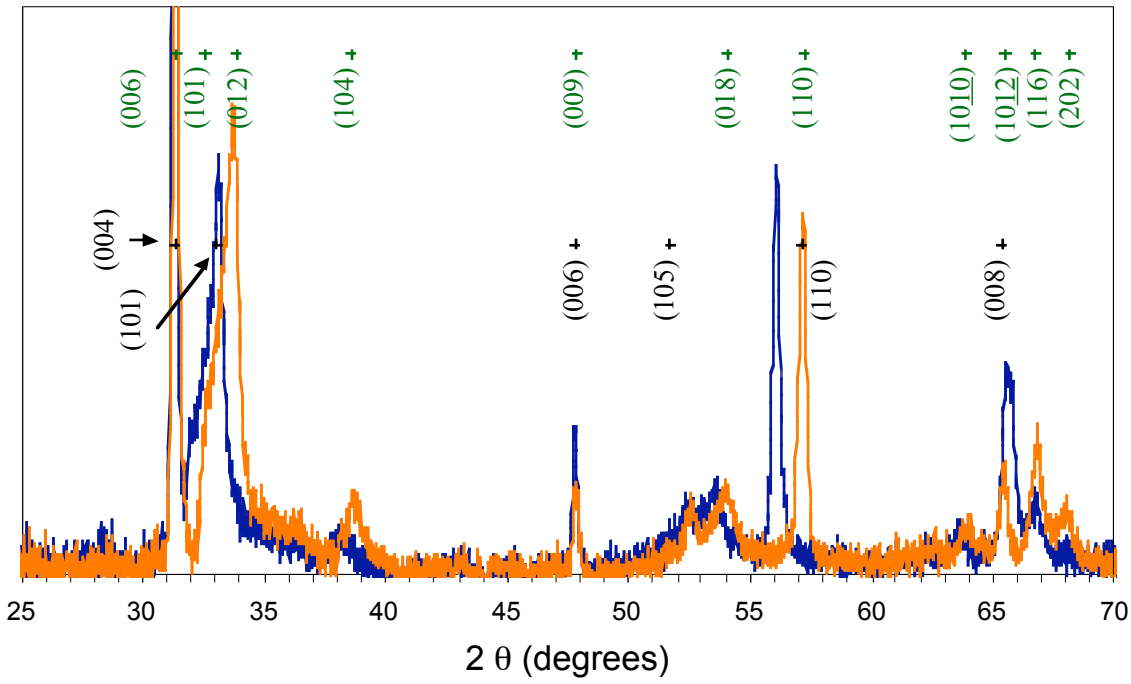

FIG. 3.3. (Color online) X-ray diffraction patterns of unoxidized $CuSc_{0.99}Mg_{0.01}O_2$ (light/orange line) and oxidized $CuSc_{0.99}Mg_{0.01}O_{2.5}$ (dark/blue line) films. The important reflections of the 3R (above) and 2H (below) polytypes are indicated by crosses.

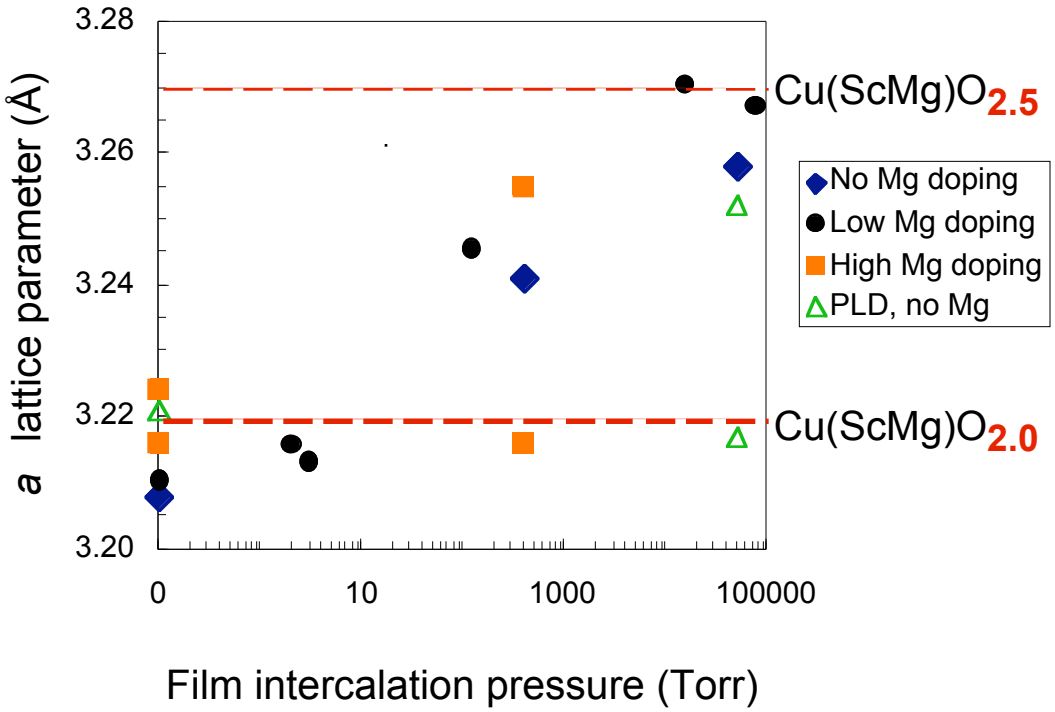

FIG. 3.4. (Color online) Variation of the *a*–axis lattice parameter in $CuSc_{1-x}Mg_xO_{2+y}$ sputtered films (closed symbols) as a function of intercalation pressure. Films were intercalated at 400˚C for ≈ 9 hours. For comparison, films made by pulsed laser deposition are included (open symbols). The *a*-axis parameters for bulk $CuScO_{2+y}$ for $y = 0$ and $y = 0.5$ are indicated by dashed lines.

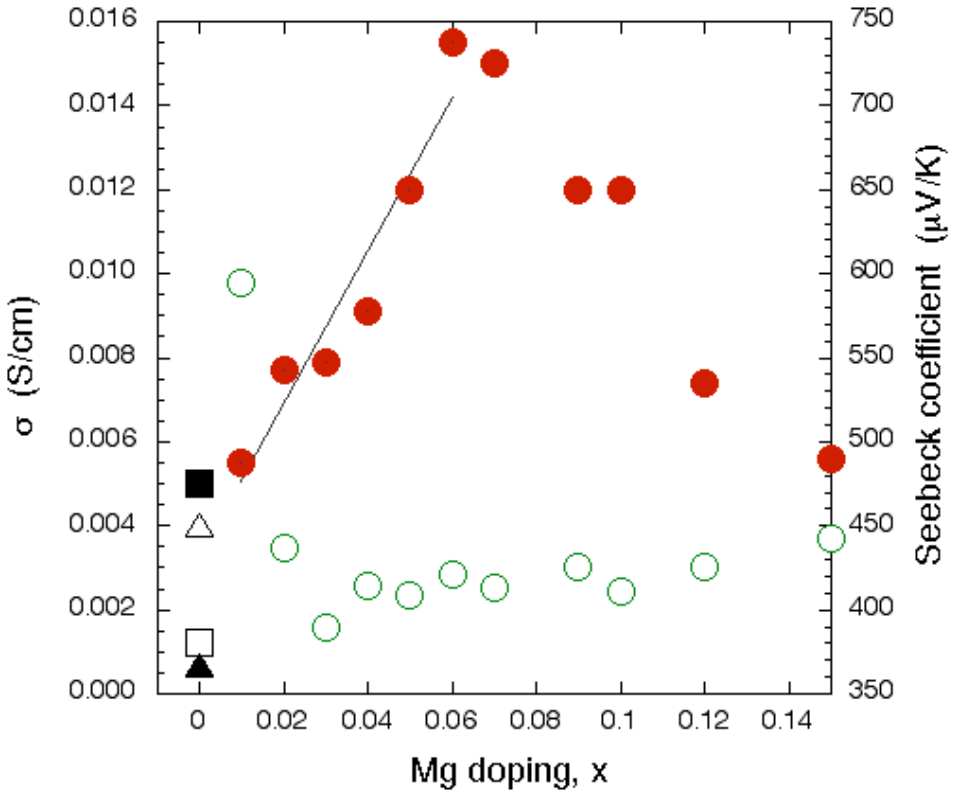

FIG. 3.5. Room temperature conductivity (closed symbols, left scale) and Seebeck coefficient (open symbols, right scale) of unoxidized $CuSc_{1-x}Mg_xO_2$ pellets. Circles correspond to Mg-doped material, squares to 2H $CuScO_2$, and triangles to 3R $CuScO_2$. The line is a fit to the conductivity data for $0.01 < x < 0.06$.

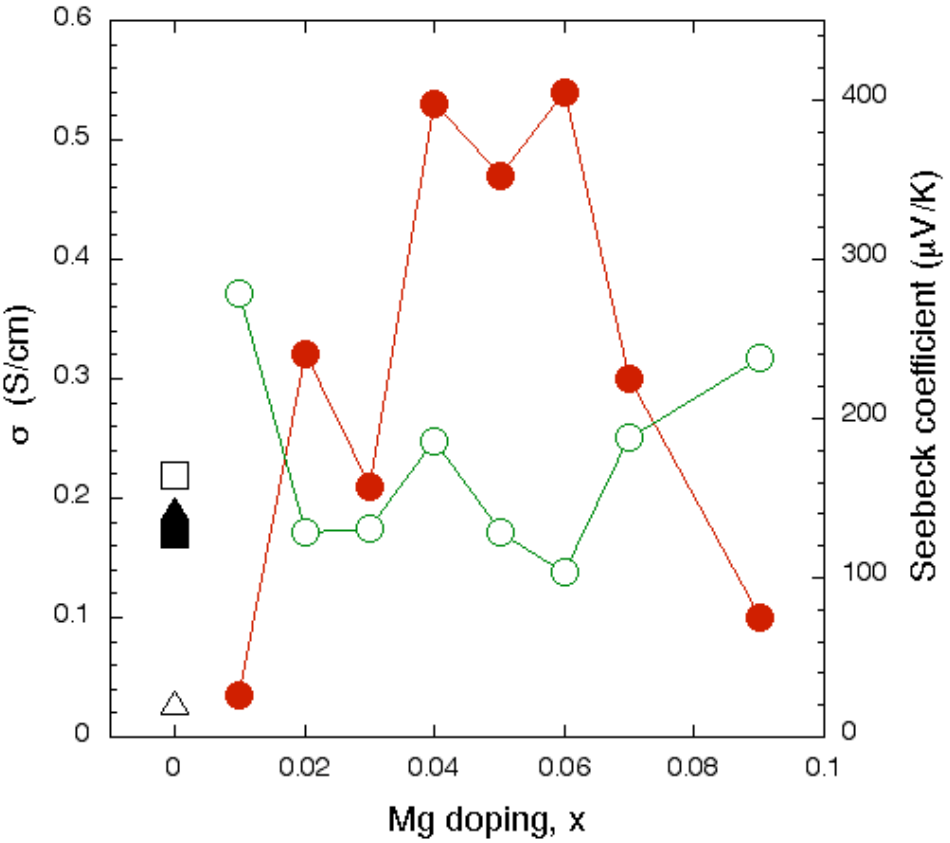

FIG. 3.6. Room temperature conductivity (closed symbols, left scale) and Seebeck coefficient (open symbols, right scale) of oxidized $CuSc_{1-x}Mg_xO_{2+y}$ pellets. Circles correspond to Mg-doped material, squares to 2H $CuScO_{2+y}$, and triangles to 3R $CuScO_{2+y}$.

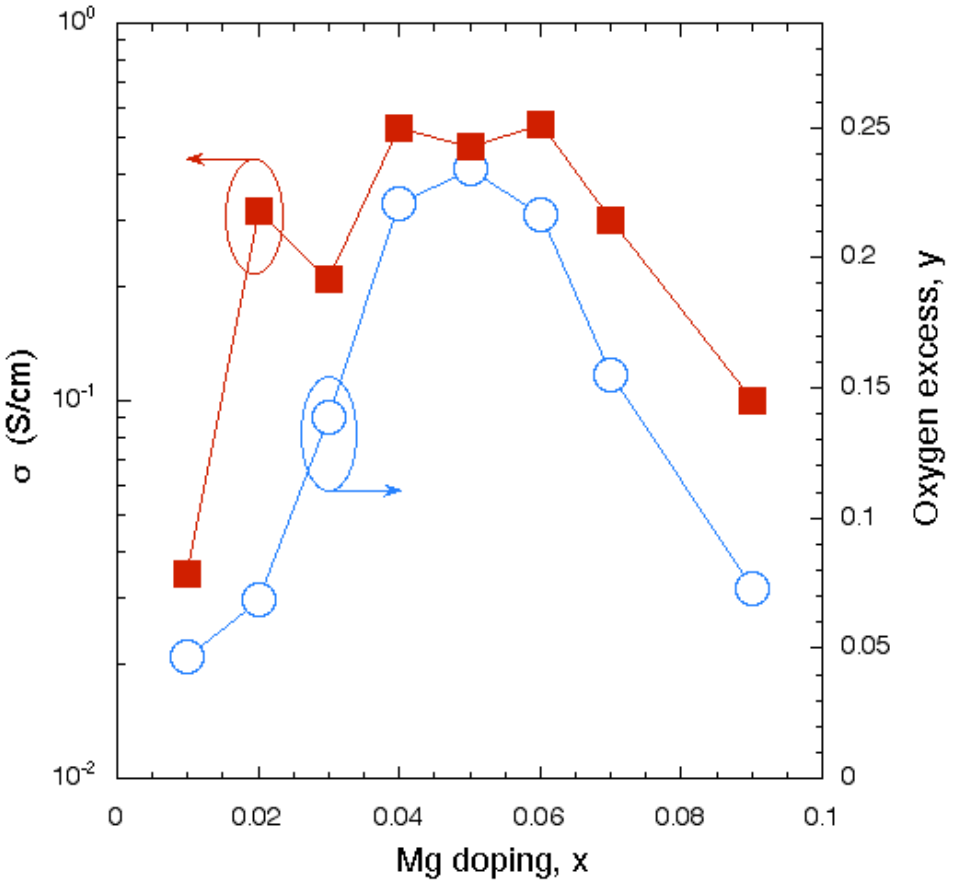

FIG. 3.7. Room temperature conductivity (closed symbols, left scale) and oxygen content as determined by TGA (open symbols, right scale) of oxidized $CuSc_{1-x}Mg_xO_{2+y}$ pellets as a function of Mg dopant concentration.

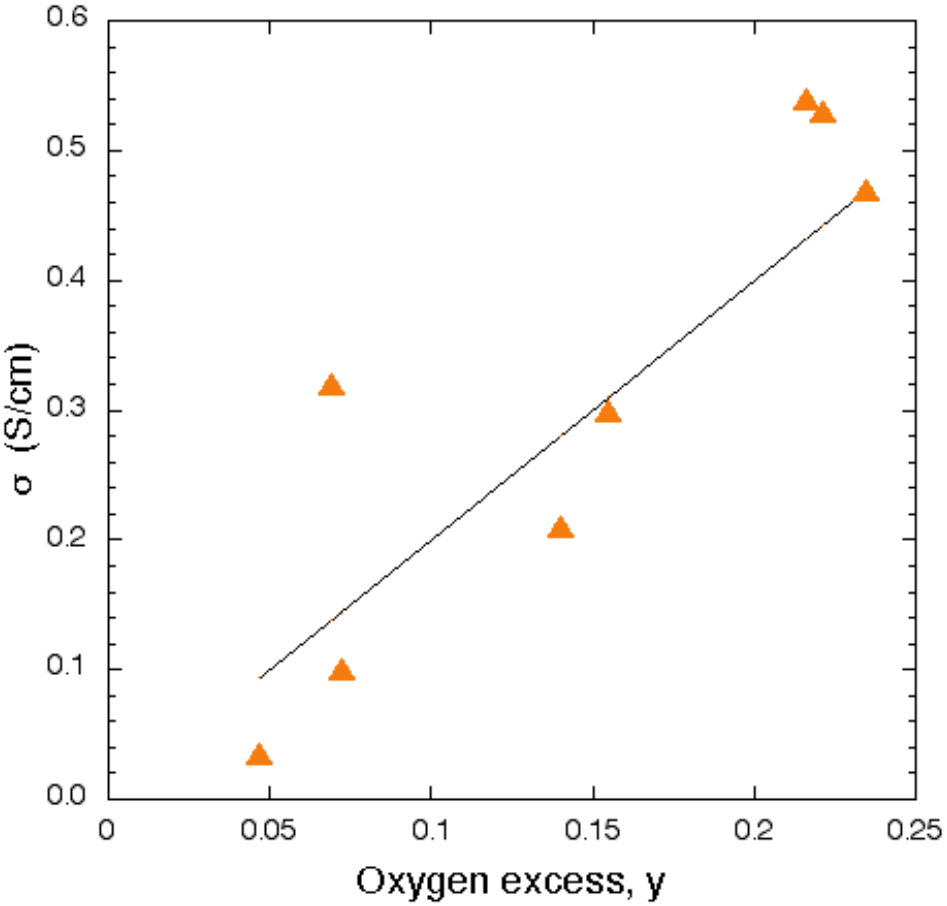

FIG. 3.8. Room temperature conductivity of oxidized $CuSc_{1-x}Mg_xO_{2+y}$ pellets as a function of average excess oxygen content. The conductivity of each corresponding unoxidized sample has been subtracted. The straight line is a fit.

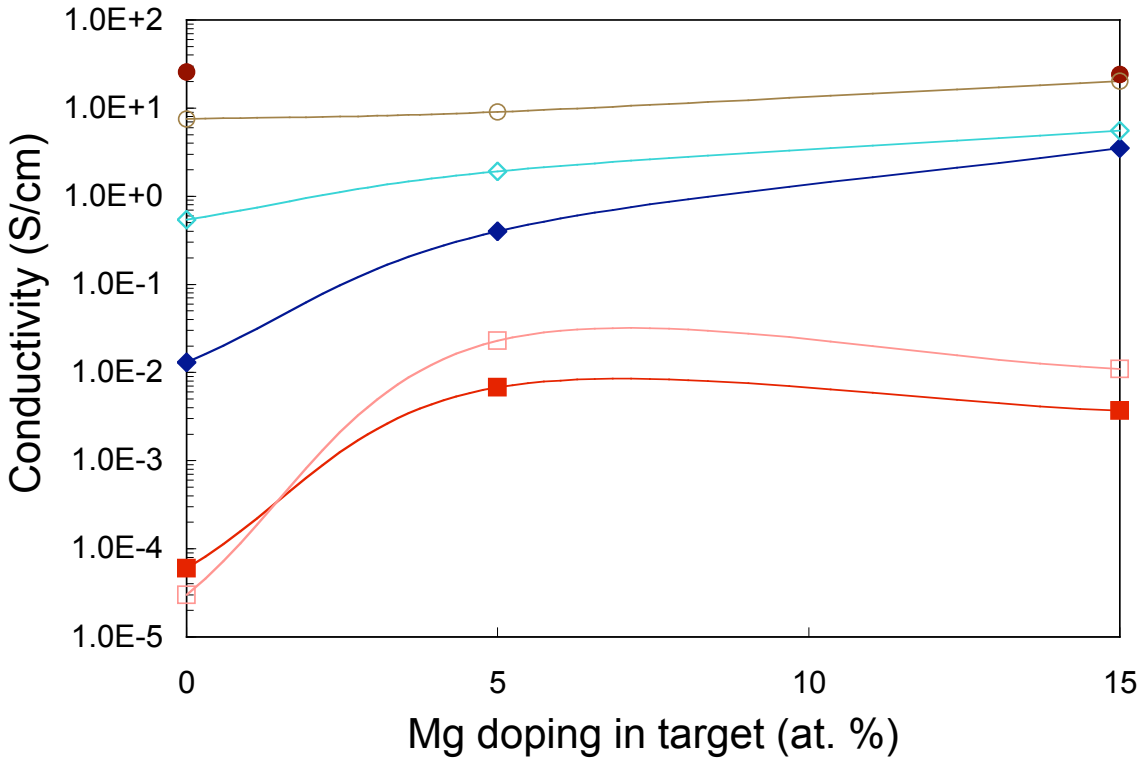

FIG. 3.9. Room temperature conductivity of $CuSc_{1-x}Mg_xO_{2+y}$ films. The Mg content is indicated as the percentage of Mg in the sputter target. Three different intercalation procedures are indicated - high pressure (circles), intermediate pressure (diamonds), and no intercalation (squares), and two different deposition temperatures – 350˚C (closed symbols) and 150˚C (closed symbols). The lines are guides.

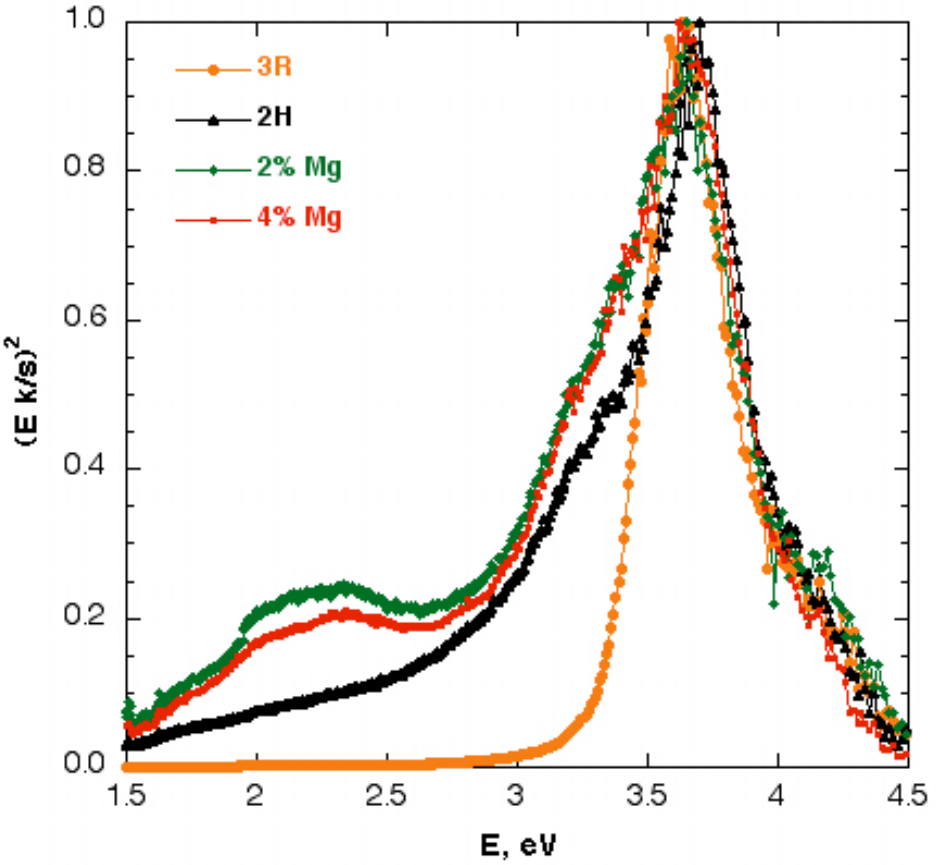

FIG. 3.10. Diffuse reflectance spectra of $CuSc_{1-x}Mg_xO_2$ powders.

3.2. Further results

3.2.1. Structural properties

Structure refinement reveals that the *a* lattice parameter decreases by about 0.04% (fig.3.11, a) upon the incorporation of the smaller Mg atom on the Sc site compared to the 2H polymorph. The *c* lattice parameter changes even less (~0.006 %) shown on fig.3.11 (b). Therefore, the incorporation of Mg on the Sc sites does not have much influence on the crystalline lattice parameters. This can be explained by the similar values of the ionic radii (~3% different) of Sc (0.745 Å) and Mg (0.720 Å) in six-fold coordination [56].

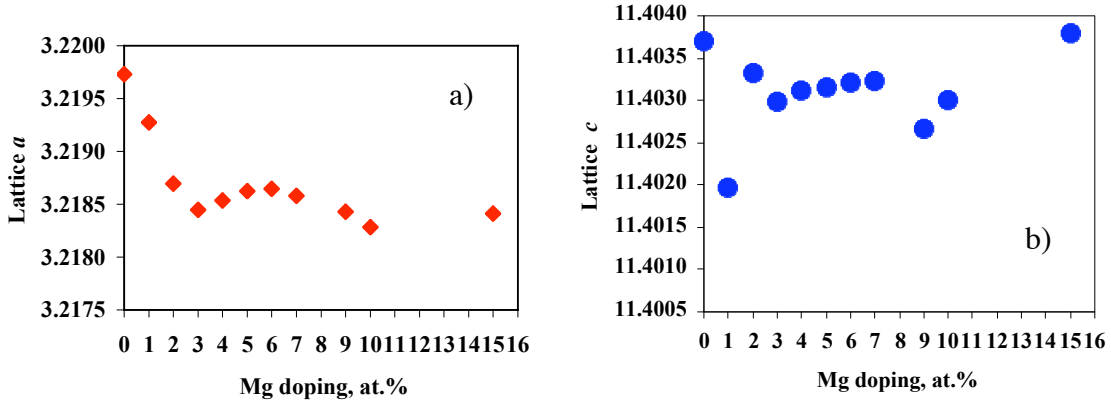

Fig.3.11. Doping with Mg on the Sc site changes the *a* lattice parameter (a) and *c* lattice parameter (b) (Jun Li).

The 3R polymorph was obtained only when no Mg was incorporated and a slight Sc excess was present, while the 2H polymorph results upon Mg doping or even in the presence of excess Cu (Fig.3.12). The structural similarities between the Mg-doped and the "Cu-doped" material indicates that the excess Cu necessary to stabilize the 2H phase substitutes as Cu^{2+} on the Sc^{3+} site.

The oxygen intercalation level of the $CuSc_{1-x}Mg_xO_{2+y}$ samples was measured by TGA (Fig.3.13). As discussed above, regardless of the simultaneous oxidation process of

all Mg doped samples, a maximum intercalation level of y around 0.22 is observable for $CuSc_{1-x}Mg_xO_{2+y}$, 0.04<x<0.06, which also show the highest conductivity values.

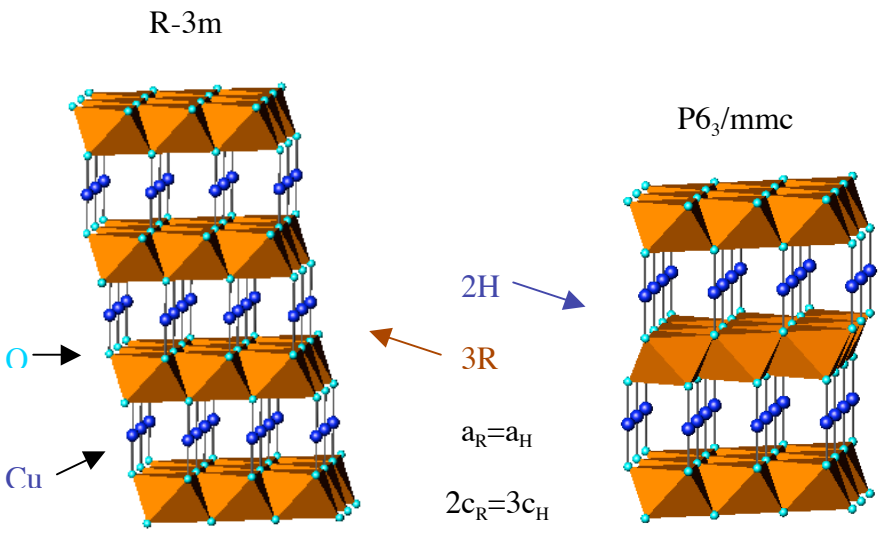

Fig.3.12. 2H and 3R polymorths of $CuScO_2$. Sc is in the center of the octahedra.

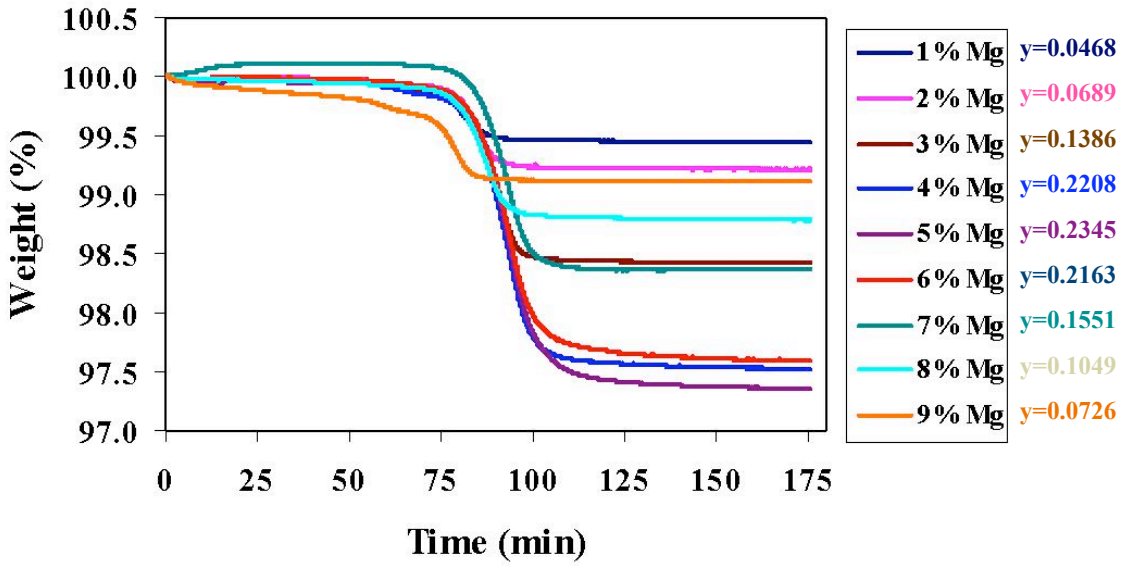

Fig.3.13. Oxygen intercalation levels of $CuSc_{1-x}Mg_xO_{2+y}$ measured by TGA. (Jun Li)

3.2.2. Electrical properties

Temperature dependent conductivity measurements were performed (Fig.3.14), and reflect dominantly VRH character. The T_0 parameter values are extracted in the 160 K - 290 K temperature range and are shown in Table 3.1. Below 160 K a change in slope is observed, leading to an even higher hopping parameter T_0, indicating further depopulation of the impurity states.

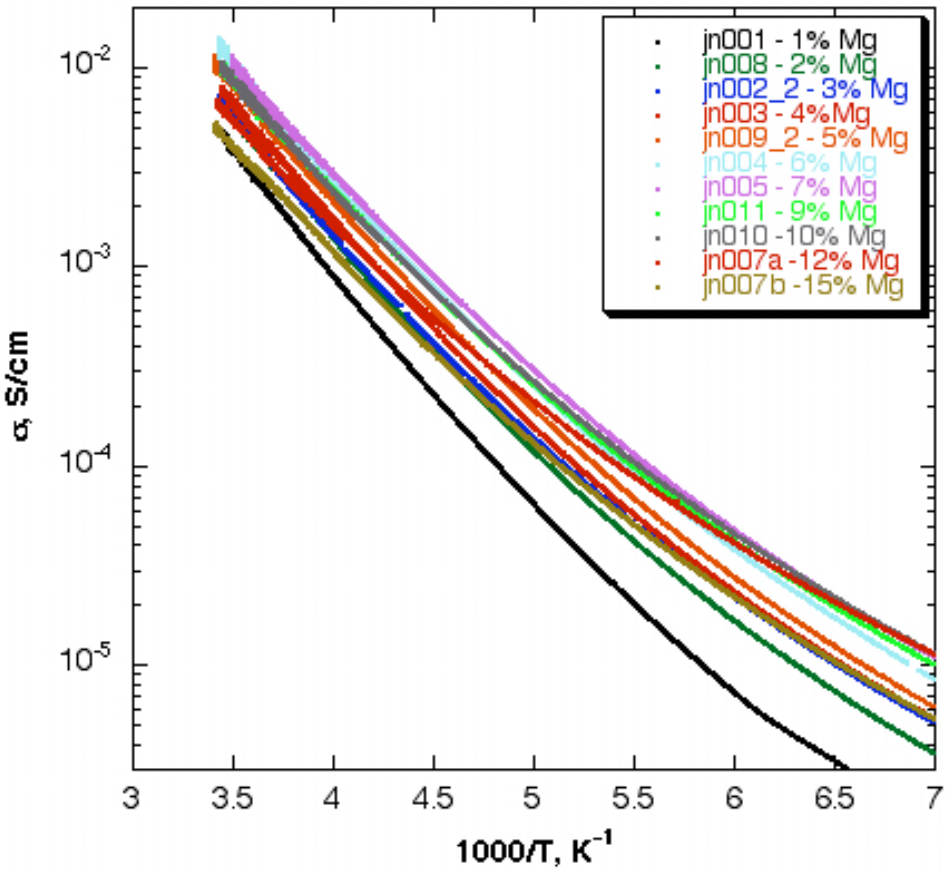

Fig.3.14. Temperature dependent conductivity measurements of not oxidized $CuScO_2$:Mg samples. The carrier activation energies decrease with increasing Mg concentration.

The conductivity of all oxidized materials is less temperature dependent (Fig.3.15) and result in lower T_0 parameter values at temperatures <180 K compared to

the unoxidized $CuScO_2$:Mg. The transport mechanism also changes to activated behavior most likely due to the appearance of broader impurity band from the incorporated oxygen, thus a higher carrier concentration available for electrical transport with somewhat higher "mobility". This is no surprise, since oxygen incorporation occurs to much higher level then Mg substitution, theoretically providing two positive carriers per incorporated oxygen.

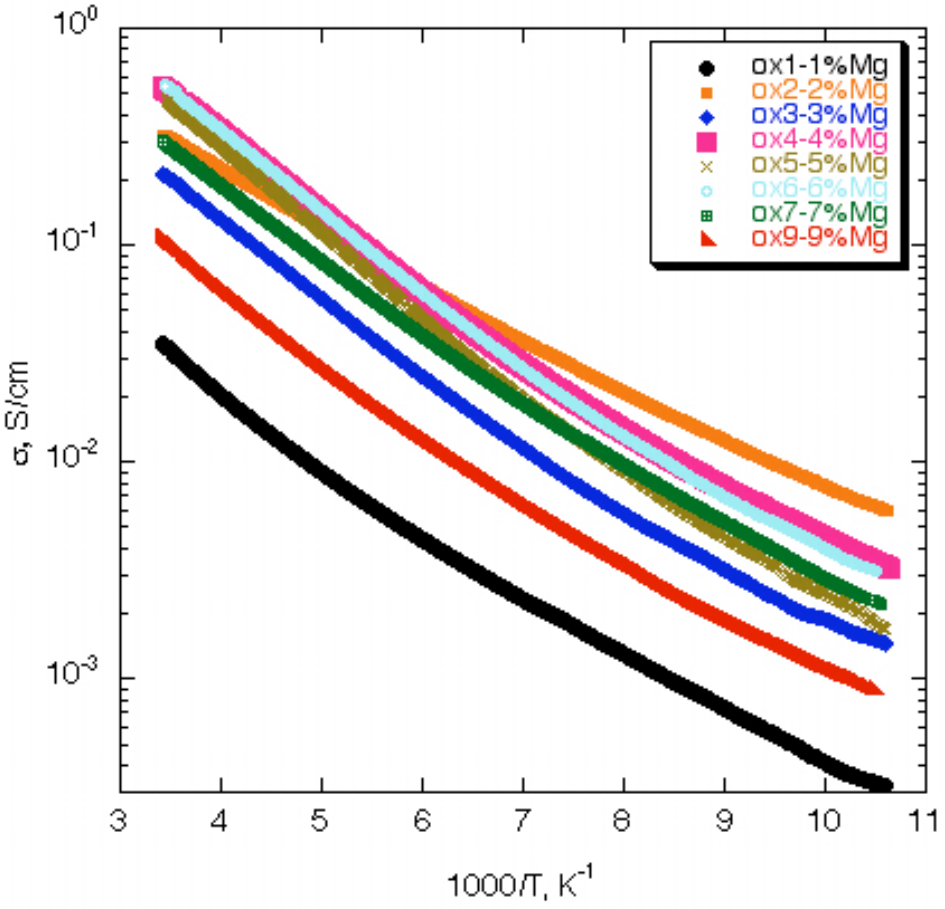

Fig.3.15. Temperature dependent conductivity measurements of oxidized $CuScO_{2+y}$:Mg samples. The activation energies are about 70 meV.

For bulk transport measurements the density of the pressed powder pellet is important, since the presence of grain boundaries greatly influence the outcome of the measurement. The desired densities lie above 60-65 % of the theoretical density of the

material, such that the conductivity measurements reflect a lower limit of the actual value of single crystalline or thin film properties. As can be seen in Fig.3.16.a, the unoxidized samples have densities above 75%. This is due to the possibility of high temperature preparation of the samples (1150°C), and in principle can be further improved by optimization of preparation conditions. Even though the trends in the conductivity and pellet densities look similar, no evidence of correlation between the two was found.

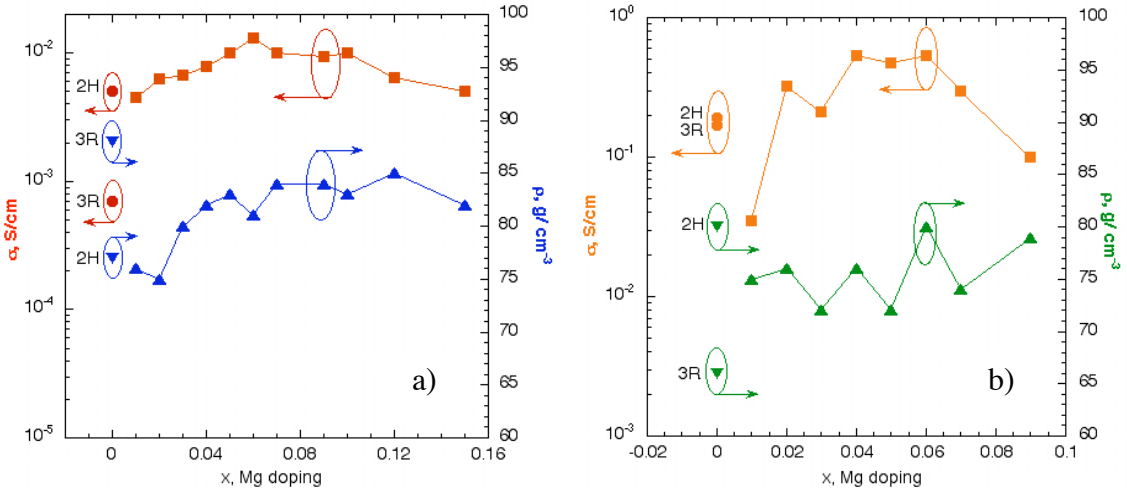

Fig.3.16. The conductivity of the samples is not noticeably correlated with their densities. Shown are a) not oxidized and b) oxidized samples.

In the case of oxidized samples, the intercalation temperature of 400°C was also the sintering temperature of the powders. This resulted in somewhat lower pellet densities (Fig.3.16 b) of 70-80 %. Again, no correlation between the densities and conductivities of the different samples was observed.

To test the importance of sintering, a pressed but not sintered sample and pressed under the same conditions and sintered sample of 2H $CuScO_2$ were prepared with densities of 80 % and 89 % respectively. Although the difference in the densities was small, the conductivity of the sintered sample was 4 orders of magnitude higher than for the unsintered one.

The temperature dependent Seebeck coefficient was studied in a few delafossite-derived compounds, $CuRO_{2+y}$ (R=La, Eu, Y etc.) [47], and variable range hopping character

was concluded. The temperature dependent Seebeck coefficient of $CuScO_{2+y}$ thin films (Fig.3.17) prepared by rf sputtering described in detail elsewhere [59], were measured. The films were intercalated at pressures between 400-40,000 Torr at 400°C in O_2 atmosphere for 12 hours. The conductivity, as well as the Seebeck coefficient, of the films are greatly dependent on the amount of intercalated oxygen and can be tuned between $1 \cdot 10^{-5}$-$3 \cdot 10^{1}$ S/cm, and 40-600 μV/K.

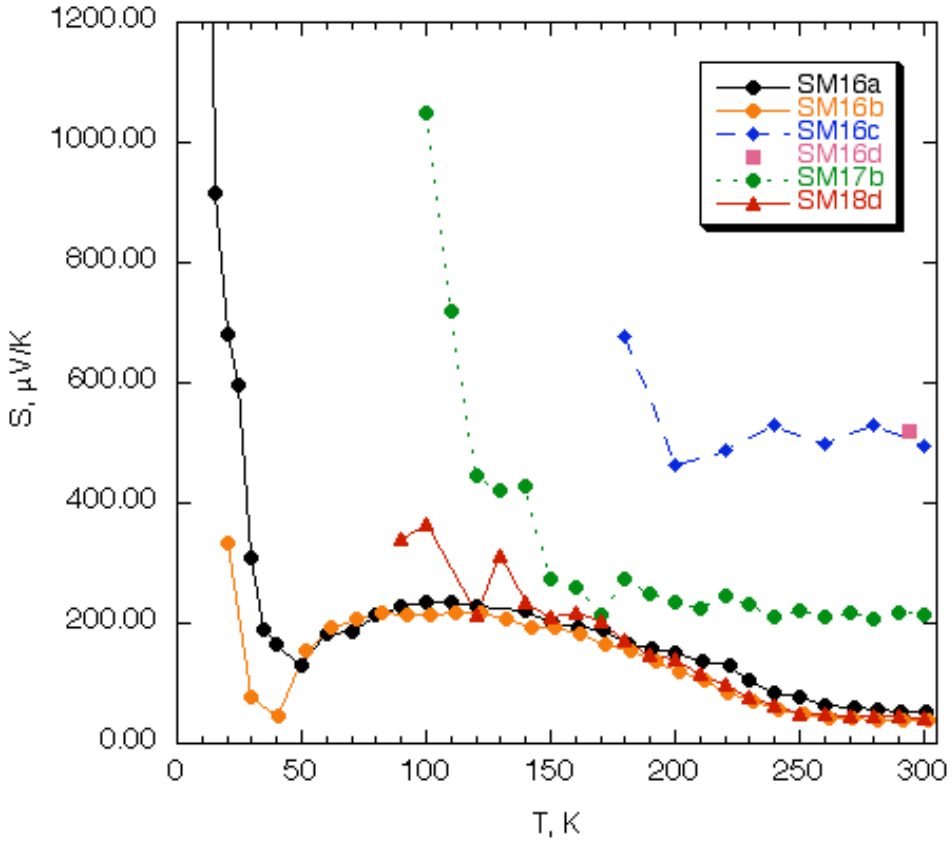

Fig.3.17. Temperature dependent Seebeck coefficient measurement of $CuScO_{2+y}$:Mg thin films between 10-300 K. The two most conductive films show a minimum around 40-50 K.

The films labeled SM16a and SM16b are the most conductive films, while SM16d is the least conductive one. All films show an increasing Seebeck coefficient down to about 100 K. This is a typical behavior for semiconducting materials with hopping type

conductivity. For the two most conductive films (highest intercalation pressures) the measurement was possible down to ~10 K, where some interesting behavior is observed. The drop in the coefficient value below 100 K is followed by a minimum around 45 K. Such a decrease in the coefficient with temperature usually indicates metallic type behavior. There is not enough information on the properties of these films at temperatures below 100 K to argue the possibility of a metallic phase formation. The following sharp increase might indicate an insulating phase/state formation of $CuScO_2$ films at such low temperature. Although, usually the Seebeck coefficient is hard to measure in the case of insulating materials, because of the lack of mobile carriers (that is why only one data point present for the SM16d sample), which doesn't seem to be the case.

A theoretical model to describe the change of the Seebeck coefficient with temperature from a statistical approach is under development by Dr. A. Wasserman and Dara L. Easley. This model, based on hopping of localized fermions, fits the measured temperature dependent Seebeck coefficient fairly well by varying an energy parameter of the localized impurity states. By varying the carrier concentration per Cu site, which is equivalent to the oxygen intercalation level, the trend of increasing Seebeck coefficient towards lower carrier concentration (intercalated oxygen) can be obtained. This theory is under development towards more fundamental description of the energy parameter, used in the model [60].

3.2.3. Optical properties

The optical properties of unoxidized and oxidized $CuScO_2$:Mg as well as the 3R and undoped 2H phases were measured by the diffuse-reflectance technique. The 3R phase material is slightly gray in color and its band gap was estimated at about 3.3 eV and is close to the values measured in thin films (3.6 eV). The undoped 2H phase $CuScO_2$ powder is dark gray and the additional feature in diffuse-reflectance around 3.3 eV can be clearly recognized. Incorporation of Mg into the samples further darkens the material. The band gap of the material seems not to change by conversion to the 2H phase and

introduction of Mg but rather scattering centers are being created which compromise the transmittance. The powder colors are shown in fig.3.18.

The oxidation process converted all our $CuScO_2$ samples to black powders. It is well known to decrease the transmittance in thin films, too. The absorption in the materials is so high, that band gap properties cannot be observed (Fig.3.19). In principle, more information can be obtained for the oxidized materials, by mixing the highly absorbing $CuScO_{2+y}$:Mg powders with non- or low-absorbing material, so that higher flux is established through the detector.

Fig.3.18. Powder colors of the intercalated 3R $CuScO_2$ (left), unoxidized 3R and 2H polytypes, and 4 at. % Mg doped.

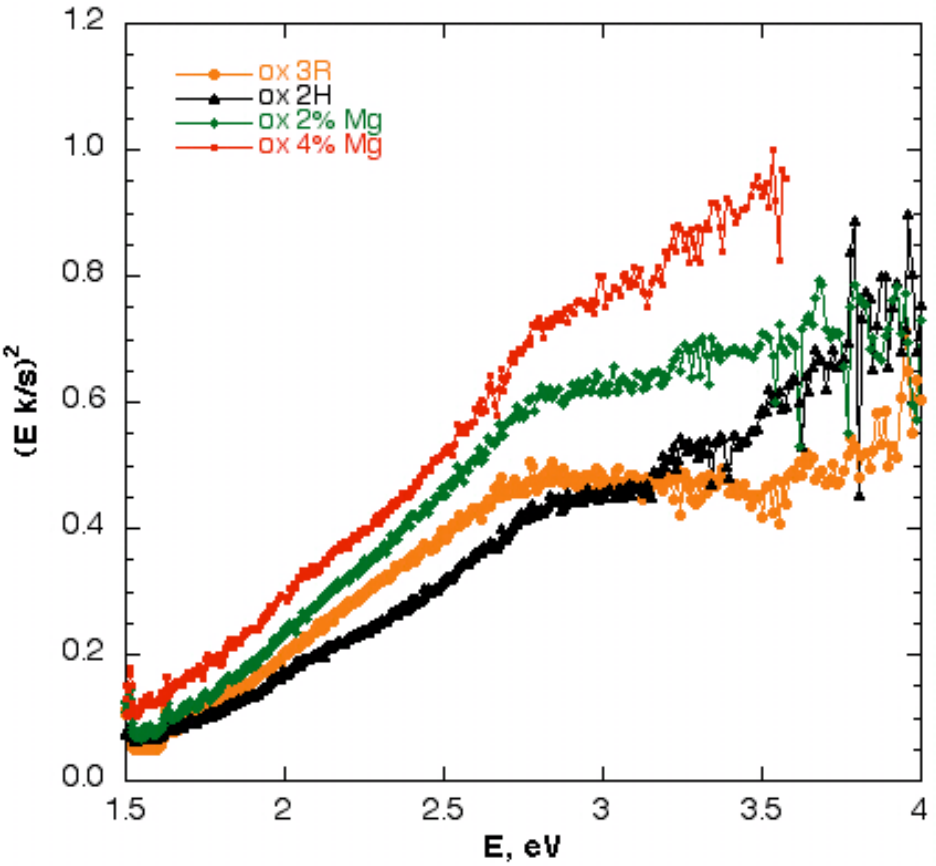

Fig.3.19. Oxygen intercalation makes $CuScO_{2+y}$ black, hence no band gap structure can be observed via diffuse reflectance.

3.4. Conclusions

The possibilities and influence of doping on the structure and transport properties on a subset of compounds of the delafossite structure are explored in this work. Both, Mg and intercalated oxygen, are proved to be effective dopants in $CuScO_2$.

A systematic study of the effect of Mg doping on the properties of $CuScO_2$ is carried out. It is shown that the Mg enters the crystalline lattice substitutionally on the octahedral Sc site and stabilizes the 2H polymorph of the compound. The temperature dependent electrical conductivity measurements indicate variable range hopping type mechanism of carrier transport. The possible influence of the pellet densities on the

results of conductivity measurements are ruled out because no correlation between them is found and the trend is further supported by Seebeck coefficient measurements.

The intercalated oxygen is shown to take interstitial sites in the Cu plane of the crystalline lattice, expanding the *a*-lattice parameter. It is established that the oxygen can be incorporated in larger amounts (up to $CuScO_{2.5}$) then Mg, and a further increase in the conductivity of the compound to 0.5 S/cm is observed. Thermally activated behavior is observed above 200 K, indicating higher carrier concentration and broader impurity bands. The highly increased absorption level of the intercalated $CuScO_{2+y}$ is a significant drawback for TCO applications.

Temperature dependent Seebeck coefficient measurements on thin film with varied oxygen intercalation levels show typical semiconductor like behavior, although the origin of the anomaly at low temperatures is not understood.

Chapter 4. Properties of bulk $BaCu_2(S,Se)_2$ and $BaCu_2(S,Se)_2$:K

4.1. Introduction

Unsuccessful attempts at producing highly transparent and conductive oxide systems have led to the chemical design of new ternary and quaternary compounds of oxy-sulfide, sulfide and sulfide-fluoride based materials. These might be the most suitable choices (oxy-sulfides and sulfide-fluorides) for preserving transparency in the visible region, since the heavier chalcogenide atoms (Se, Te) are found to decrease the optical band gap of the compound. Such band gap modulation in $BaCu[Q_{1-x}Q'_x]F$ solid solutions, where a continuous change from 3.1 eV (BaCuSF) to 2.9 eV (BaCuSeF) via increasing amounts of Q' = Se with Q = S, and a further decrease in the [Se,Te] solid solutions [61] to 2.3 eV for BaCuTeF [62], is already observed. The band gap modulation is an important feature in a material system for possible band edge excitonic emission, as have been observed in the LaCuOS [63] compound, and modulated in the $LaCuOS_{1-x}Se_x$ solid solutions [64].

It is also commonly observed that heavier chalcogenide atom substitution in the materials mentioned above causes a significant increase in the conductivity, although they lose optical transparency. This can be attributed to more covalent bonds forming between S or Se and Cu compared to oxygen, also observed in the $BaCu_2Q_2$ (Q=S, Se, Te) ternary systems. The more covalent bonds (and larger chalcogenide atoms) lead to higher dispersion near the top of the valence band, giving rise to higher mobility and hence improved conductivity, but also decreasing the gap between the bands. For example, the conductivity increases by almost two orders of magnitude when Se substitutes S in LaCuOQ [64] epitaxial films. In BaCuQF bulk pellets, BaCuSeF has a somewhat lower conductivity than BaCuSF [65], but more definitive results are expected from high quality thin films where grain boundaries are less important. . Upon doping on the cation site (Mg for La, or K for Ba), both material systems show improved conductivity (up to ~100 S/cm) and the temperature dependent conductivity becomes typical of a degenerate semiconductor.

$BaCu_2S_2$ and $BaCu_2Se_2$ are highly conductive p-type semiconductors. The former can be prepared in two phases, a low temperature orthorhombic form, α-$BaCu_2S_2$ [66] (Fig.4.1, a), and high temperature tetragonal form, β-$BaCu_2S_2$ [67] (Fig.4.1, b), determined form single crystal XRD. The latter has been synthesized only in the tetragonal form, so far. These materials have not received wide attention and only basic structural and electrical properties have been studied. It was shown, though, that the $BaCu_2S_2$ has a typical semiconductor like behavior [66] and upon high potassium doping ($Ba_{1-x}K_xCu_2S_2$, $x \geq 0.2$) [68] the compound exhibits metallic type behavior. The Cu deficient ($BaCu_{2-x}S_2$ $0<x<2.0$) compound also exhibits increasing conductivity [69], which might indicate that the hole carriers are created by Cu vacancies.

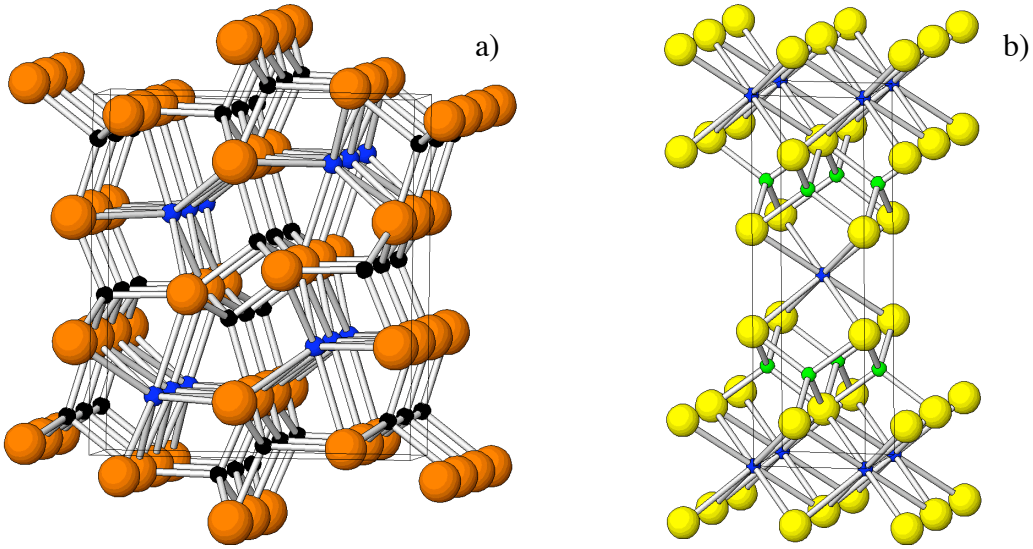

Fig.4.1. Structure of (a) α- and (b) β-$BaCu_2S_2$.

Another interesting feature of the $BaCu_2Q_2$ (Q=S, Se, Te) materials is their high conductivity and Seebeck coefficient, which makes them candidates for thermoelectric cooling materials[34]. For example, the electrical and thermal conductivity and the Seebeck coefficient of $BaCu_2Te_2$ reported by Y.C. Wang and F. J. DiSalvo [70], yield a thermoelectric figure of merit $ZT = 0.129$. For any practical application a minimum of ZT

= 2 is required. The $BaCu_2Q_2$ compounds reported in this chapter are of much higher conductivity, therefore being possible candidates for high figure of merit materials.

The thin film form of α-$BaCu_2S_2$ was recently reported by our collaboraters. [71] The band gap of 2.3 eV does not allow for transparent coating applications. Electrical measurements reveal a p-type conductivity of 17 S/cm and a mobility of 3.5 cm^2/V s, which will be used in this chapter to estimate the carrier concentration in the K-doped $BaCu_2S_2$ bulk materials.

In this chapter the transport and optical properties of K doped $BaCu_2S_2$ and $BaCu_2Se_2$ are studied. The materials were prepared by Cheol-Hee Park of the Keszler group in the Department of Chemistry at Oregon State University

4.2. Experimental

Powder samples of undoped and K-doped $BaCu_2S_2$ were prepared by heating stoichiometric mixtures of $BaCO_3$ (Cerac, 99.9%), Cu_2S (Cerac, 99.5 %), and K_2CO_3 (Aldrich, 99.995%) at 450 °C for 1 h under a flowing stream of H_2S gas and cooling to room temperature under flowing Ar. The $BaCu_2Se_2$ powders were prepared by heating stoichiometric mixtures of BaSe (Cerac, 99.5 %) and Cu_2Se (Cerac, 99.5 %) in an evacuated silica tube at 550 ^oC for 5h. For K-doped $BaCu_2Se_2$ stoichiometric mixtures of BaSe, Cu_2Se, Se (Alfa, 99.999%), and KNO_3 (Johnson-Matthey, ACS) were heated at 500 °C for 1 h under a flowing stream of H_2 (5 %) / N_2 (95 %) mixture gas.

Each powder sample was pressed at 4500 N force into a half-inch diameter pellet and annealed at 450°C for 10 h and 650°C for 1.5 h in an evacuated silica tube to obtain the α- and β-phases, respectively, of $BaCu_2S_2$. The same force is used to obtain pressed pellets of $Ba_{1-x}K_xCu_2Se_2$, $0 < x < 0.1$, with same heating procedure as for powder preparation. The resulting pellets are orange-brown in the α- $BaCu_2S_2$, dark gray-black in the case of β-$BaCu_2S_2$, $Ba_{1-x}K_xCu_2S_2$ and $Ba_{1-x}K_xCu_2Se_2$, with $0 < x < 0.1$.

All samples were characterized by powder x-ray diffraction (Cu Kα radiation) on a Siemens D-5000 powder diffractometer.

The pellets were characterized by collinear four-probe temperature dependent conductivity, Seebeck coefficient and diffuse reflectance measurements. Due to the high conductivity of the material, metal contacts were not used. The room temperature conductivity measurements were carried out using the van der Pauw method.

$BaCu_2S_2$, $BaCu_2Se_2$ and their potassium-doped derivatives are stable in ambient atmosphere and no evidence of water sensitivity is found.

4.3. Results

The optical (band gap) and transport (conductivity, Seebeck coefficient and estimate of carrier concentration) properties of the $BaCu_2S_2$ pressed powder samples discussed in this section are summarized in Table 4.1. The carrier density, n, was calculated assuming a mobility of 3.5 cm^2/Vs.

Table 4.1. Transport and optical measurements results of $Ba_{1-x}K_xCu_2S_2$, $0 < x < 0.1$.

$Ba_{1-x}K_xCu_2S_2$	σ, S/cm	S, μV/K	$n_{calculated}$, cm^{-3}	Band Gap, eV
x=0, α-	1.7	197	$3 \cdot 10^{18}$	2.3
x=0, β-	19	226		1.75
x=0.005	34	228	$1.7\ 10^{19}$	1.75
x=0.025	119	150	$2.05\ 10^{20}$	1.75
x=0.05	263	132	$3.15\ 10^{20}$	1.75
x=0.075	370	112	$5.45\ 10^{20}$	1.75
x=0.1	434	101	$6.95\ 10^{20}$	1.75

4.3.1. Optical properties

Diffuse reflectance measurements (Fig.4.2) reveal a band gap of about 2.3 eV for the α-phase and a 1.75 eV for the β-phase $BaCu_2S_2$ powders, being consistent with the

orange and black colors of the samples. All samples show a direct optical gap, with no evidence of an indirect gap. Although these small bandgap values do not permit transparency over the full optical spectrum (unlike oxide based transparent conductors, ITO, $CuScO_2$, etc.), the material still could find application in appropriate solar cells and other devices because of its outstanding transport properties. Also, it is the basis for the layered BaCuQF materials, which are transparent, and show great promise as TCs, so that the "parent" compound is interesting to study.

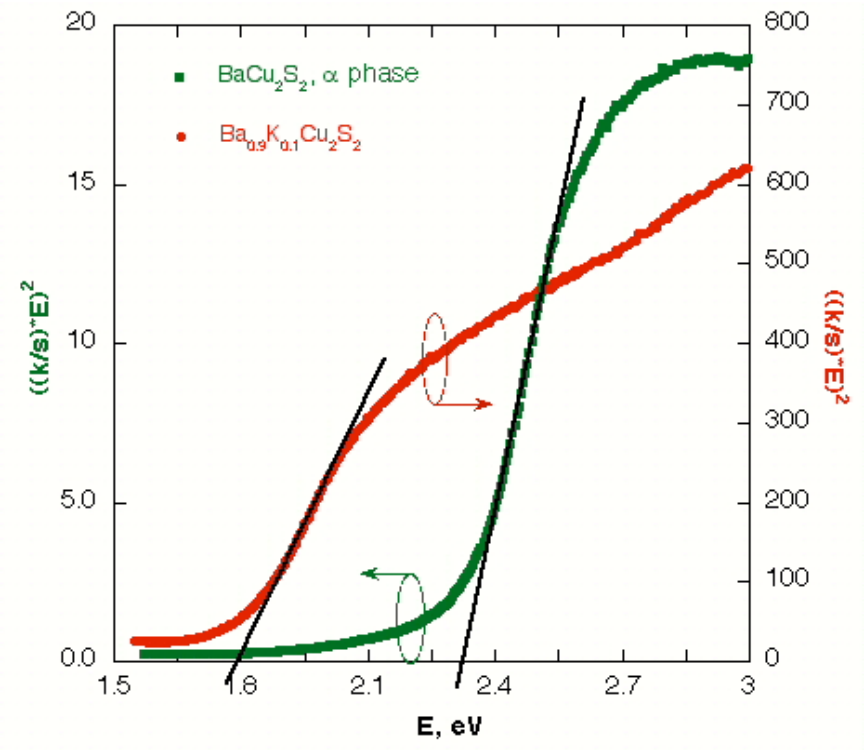

Fig.4.2. Diffuse-reflectance optical measurements for band gap determination of α- $BaCu_2S_2$ (green) and $Ba_{0.9}K_{0.1}Cu_2S_2$ (red) (Cheol-Hee Park)

4.3.2. Effect of preparation temperature

The preparation temperature dependence of $BaCu_2S_2$ and $Ba_{0.95}K_{0.05}Cu_2S_2$ were examined to verify reproducibility, influence on pellet density and transport properties.

Undoped and 5 at. % K doped $BaCu_2S_2$ pressed powders were prepared at 450˚C and their temperature dependent conductivities measured (Fig.4.3). The samples were round (dia. ~9.5 mm) and 1.5 mm thick. The room temperature conductivities were about 1.7 S/cm for the α-phase sample and about 160 S/cm for the 5 at. % potassium doped sample. The striking difference is that while the undoped sample shows activated conductivity, the doped sample conductivity increases with temperature. After the measurements the samples were heated at 650 ˚C for 1.5 hrs in an evacuated silica tube. This heat treatment converts the undoped α-phase material to the β-phase, and it increased the room temperature conductivity of the undoped sample by an order of magnitude to 20 S/cm. Since the presence of the potassium induces the β-phase even at low preparation temperature, one might expect only a slight change in the conductivity in the doped samples due to sintering at 650 ˚C. As expected, the difference is not as dramatic as in the case of the α-phase conversion, and results in a room temperature conductivity of about 210 S/cm. The temperature dependent behavior remains of the same character for each sample.

To illustrate reproducibility, properties of two sets of samples of $Ba_{1-x}K_xCu_2S_2$, $0 < x < 0.1$, prepared at 450˚C and 650˚C pellet annealing temperature are summarized in Table 4.2. The undoped $BaCu_2S_2$ and $Ba_{0.95}K_{0.05}Cu_2S_2$, which underwent both the 450˚C and 650˚C annealing procedures, are part of the high (650˚C) temperature set. Note that the densities of these two samples are lower than those of the samples prepared at high temperature directly, with x = 0.005, 0.025, 0.075, 0.1.

The characterization results show a systematically lower conductivity for lower annealing temperature, but the difference decreases with higher K doping level. Nonetheless, the higher preparation temperature of 650˚C results in powder pellets of improved conductivity and density. Of course, the higher pellet density can be responsible for the improvement of transport properties. The Seebeck coefficients of both sets of samples is very similar, indicating no dependence on density, therefore being a measurement of an intrinsic property.

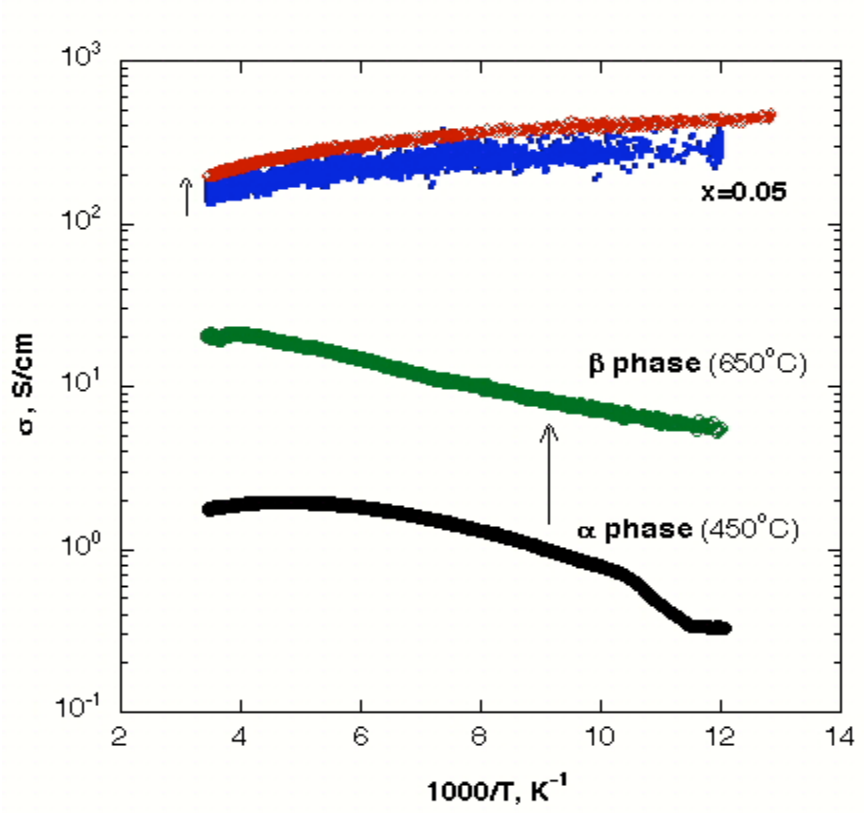

Fig.4.3. Higher preparation temperature results in more conductive materials of $BaCu_2S_2$ and K-doped derivative.

Table 4.2. Pellet density and conductivity dependence on preparation temperature of $Ba_{1-x}K_xCu_2S_2$.

Sample doping	ρ/ρ_{th}, %, 450˚C	σ, S/cm, 450˚C	ρ/ρ_{th}, %, 650˚C	σ, S/cm, 650˚C
0	-	1.7 (α-)	64	20 (β-)
x=0.005	71	9.4	84	34
x=0.025	61	83	89	119
x=0.05	69	142	72	263
x=0.075	71	256	81	370
x=0.1	65	363	83	434

4.3.3. Transport properties

Along with the undoped and 5 at. % K-doped $BaCu_2S_2$ discussed above (Fig.4.3), $Ba_{1-x}K_xCu_2S_2$ with x = 0.005, 0.025, 0.075 and 0.1 were prepared at 650˚C to form a set of samples with systematically increased potassium doping level. Their temperature dependent conductivities of this set were measured (Fig.4.4). The change from activated to metallic carrier transport mechanism takes place in samples with K doping $x \geq 0.025$. The origin of the carriers in the undoped state is unknown, but the presence of potassium induces a large number of carriers, that in turn moves the Fermi energy level toward the VB edge, resulting in degenerate semiconductors. Room temperature conductivity of up to 410 S/cm in $Ba_{0.9}K_{0.1}Cu_2S_2$ is the one of the highest among the currently known p-type TC's.

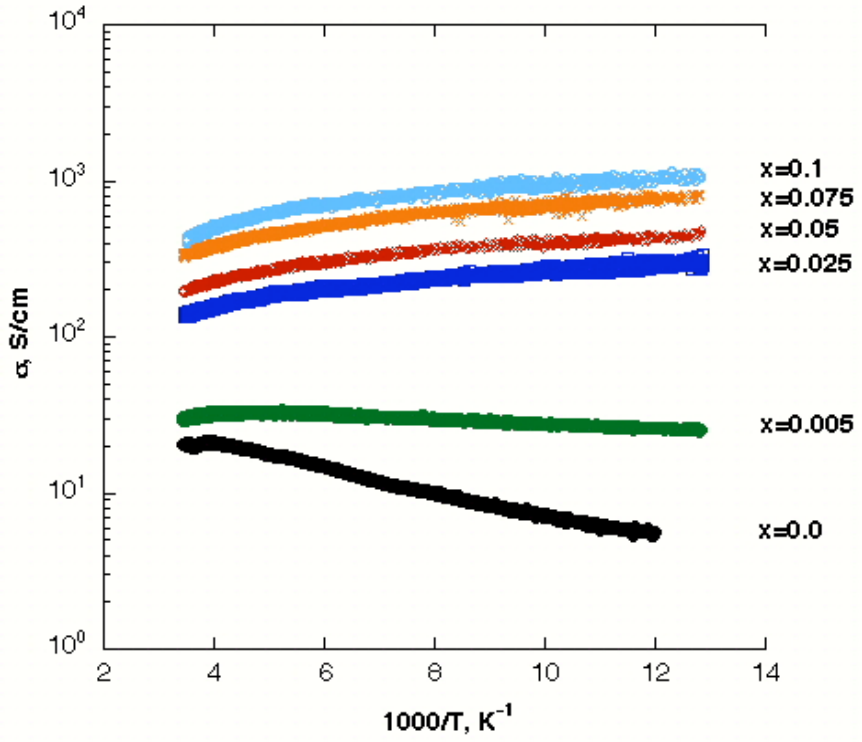

Fig.4.4. Temperature dependent conductivity measurements of $Ba_{1-x}K_xCu_2S_2$. Activated behavior is observed in the undoped form (x=0). K doped samples with x > 0.005 show degenerate semiconductor behavior.

A carrier concentration calculation was carried out based on the assumptions that the mobility of the intrinsic carriers in the undoped material is 3.5 $cm^2V^{-1}s^{-1}$ [71] and remains unchanged with doping (Fig.4.5). Along with the measured conductivity, such a calculation yields a carrier concentration of $3.5 \cdot 10^{19}$ cm^{-3} in the undoped $BaCu_2S_2$ and increases to $7.7 \cdot 10^{20}$ cm^{-3} for 10 at. % K doping, using:

$$p = \sigma/(\mu \cdot e) \tag{4.1}$$

where σ is the conductivity of the sample, μ is the mobility of the carriers, and e is the charge carried by the carrier. The doping efficiency, i.e. the number of potassium atoms present producing a carrier, shows a maximum of 85 % at in $Ba_{0.95}K_{0.05}CuS$, and somewhat decreases with higher doping levels, indicating a limited solubility of K or

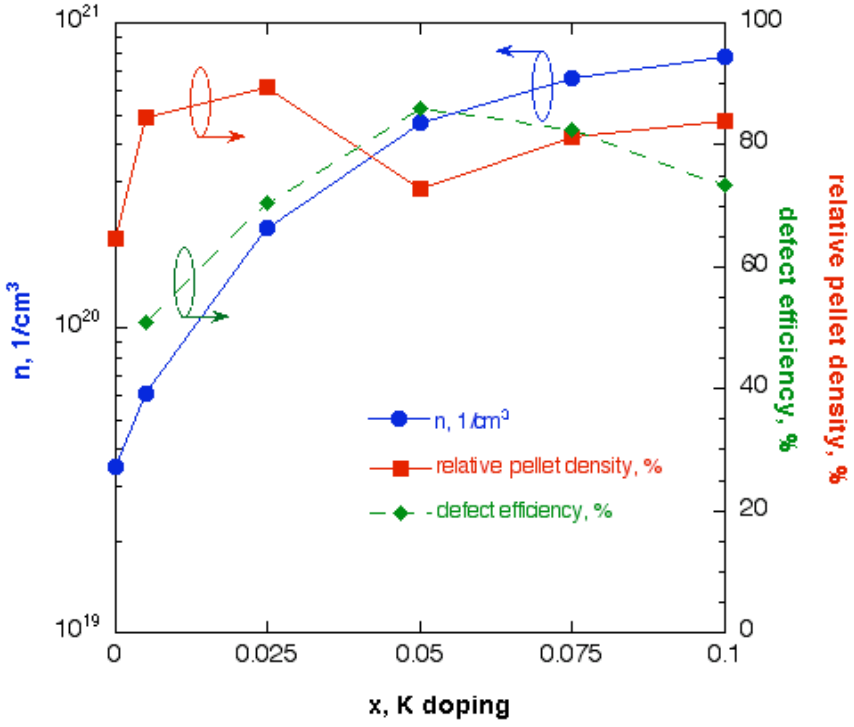

Fig.4.5. Estimated carrier density (blue) and defect creation efficiency (green) with K doping in $BaCu_2S_2$. The densities of the pressed pellets are shown in red.

increased scattering of mobile carriers on defects introduced by doping in the compound. XRD of the 5 at. % to 10 at. % potassium doped samples, show no K derived residues, which suggests that the latter scattering mechanism is more likely the cause of the decreased efficiency.

The results of room temperature conductivities and Seebeck coefficients are summarized in Fig.4.6. The Seebeck coefficient measurement results follow an expected trend: the lower conductivity sample (undoped β-phase) has the highest value and decreasing as the conductivities due to doping increase. It is interesting to note that while in the case of $CuScO_{2+y}$:Mg, where the conductivities were 1-2 orders of magnitude lower than in $BaCu_2S_2$, the Seebeck coefficient are lower or of comparable value (compare Fig.4.6 and Fig.3.6). This might be an indication of a high thermoelectric figure of merit, although thermal conductivity measurements on $BaCu_2S_2$ are not available. To achieve a ZT = 4 for this compound in thermoelectric devices, a thermal conductivity of about κ = 0.3 mW/(cm·K) would be required. For $BaCu_2Te_2$, mentioned in the introduction, a thermal conductivity of 22 mW/(cm·K) [70] was reported, which is 2 orders of magnitude higher for the same material class. Assuming this value of κ for the case of $BaCu_2S_2$ a maximum $ZT = 0.06$ can be obtained, quite low for practical application.

Even higher results for conductivity are observed in the $Ba_{1-x}K_xCu_2Se_2$ compounds. The substitution of Se for S is expected to lead to higher covalency of Cu-Se bonds, allowing for broader impurity bands, and perhaps improved carrier mobility. Indeed, the measured conductivities of this compound are higher then that of $Ba_{1-x}K_xCu_2S_2$, by at least a factor of 2 or more (Fig.4.7). This is a quite substantial improvement, since in the potassium doped samples with x = 0.1, σ = 420 S/cm for the sulfur based compound and σ = 750 S/cm in the selenium compound. This is the highest achieved conductivity in pressed powder p-type conductors. The compound promises a high figure of merit, although the Seebeck coefficient for the highly conductive samples is low. The estimated thermal conductivity for the "magic" figure of merit of $ZT = 4$ is about $1 \cdot 10^{-4}$ W/(cm·K), an even lower value than that for $BaCu_2S_2$:K compounds.

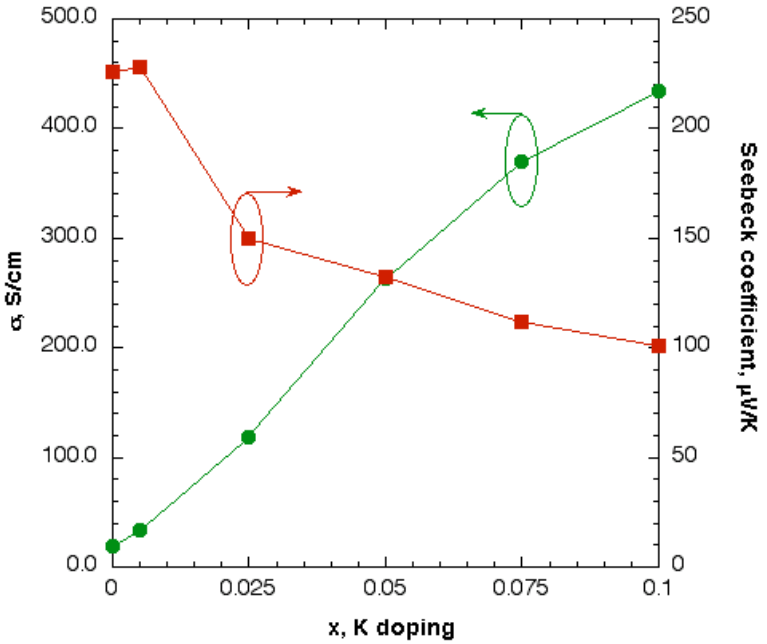

Fig.4.6. Room temperature conductivity and Seebeck coefficient of $Ba_{1-x}K_xCu_2S_2$, $0<x<0.1$.

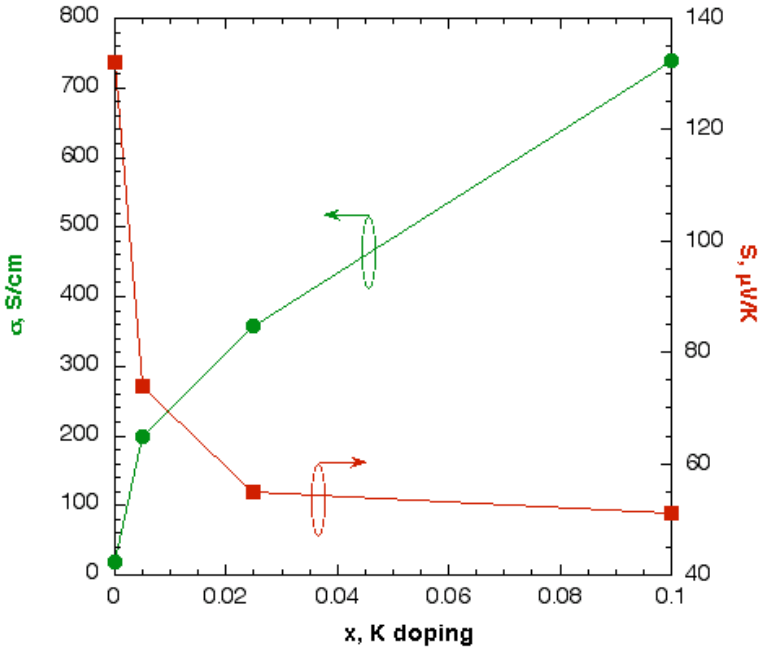

Fig.4.7. Transport properties of $BaCu_2Se_2$ at room temperature.

Temperature dependent Seebeck coefficient measurements were carried out on the undoped β-phase $BaCu_2S_2$ and $Ba_{1-x}K_xCu_2S_2$ with x= 0.005, 0.05 and 0.1 (Fig.4.8). The shown result can be fitted well by eq. 2.18 and Table 4.3 summarizes the fitting parameters. As the K doping level in $BaCu_2S_2$ increases the temperature dependence of the coefficient becomes very similar to that of metals. This is indicated by the nearly linear behavior and decreased value of the coefficient of the $Ba_{1-x}K_xCu_2S_2$ samples with x=0.05 and 0.1, compared to the undoped and lightly doped samples. This is in very good agreement with the results of temperature dependent conductivity measurements showing the same trends for these compounds. The temperature dependence can also be modeled assuming delocalized impurity states, by varying the carrier concentration (increasing towards lower curves) and an effective mass parameter [60].

Table 4.3. Fitting parameters *A*, *B*, and *C* for varying K-doping levels in $BaCu_2S_2$.

x, K-doping	*A*, μV/K^2	*B*, μV	*C*, μV/ K$^{3/2}$
0 (β-phase)	-0.506	-1229	22.4
0.005	-0.244	-492	17.3
0.5	-0.049	-227	8.3
0.1	-0.056	-131	6.7

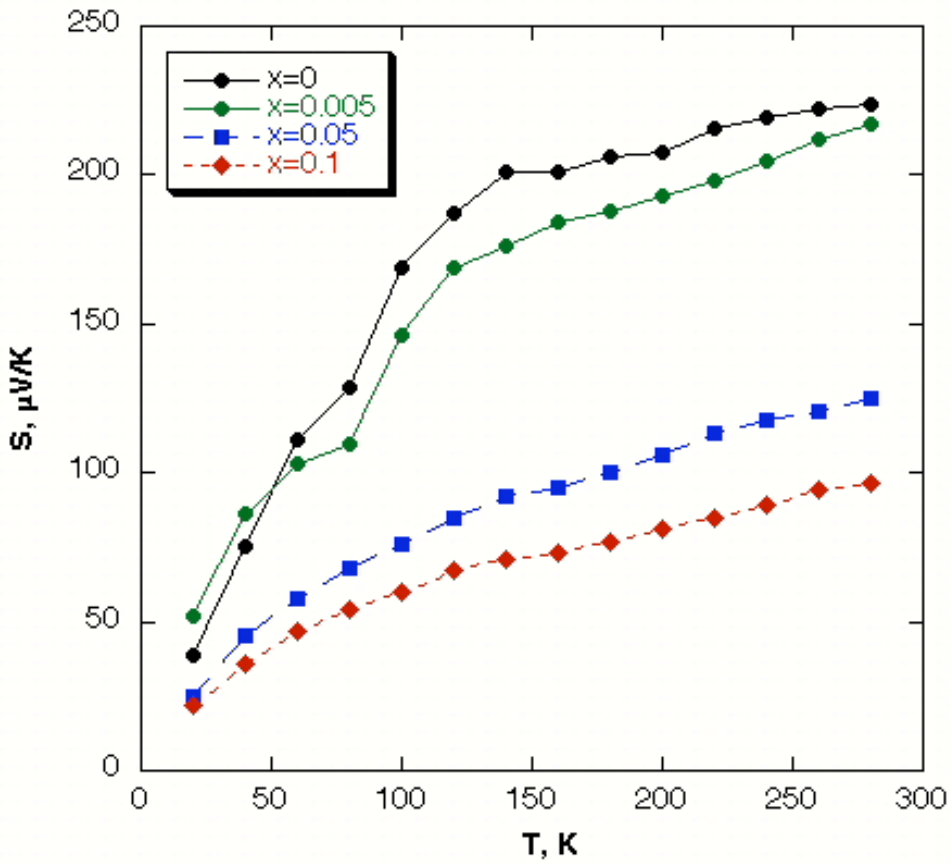

Fig.4.7. Temperature dependent Seebeck coefficient of β-$BaCu_2S_2$ and $Ba_{1-x}K_xCu_2S_2$ show increasingly degenerate semiconducting properties with higher potassium doping level, and agree well with results of temperature dependent conductivity measurements.

4.4. Conclusions

Transport properties of p-type $BaCu_2S_2$ and $BaCu_2Se_2$ and the effect of K doping are presented. The low temperature α-$BaCu_2S_2$ exhibits the lowest conductivity of 1.9 S/cm, with a band gap of 2.3 eV, and can be converted to β-$BaCu_2S_2$ with improved transport properties, but on the expense of an even lower band gap of 1.75 eV. The density of a pellet is lowered when converted from α- to the β-phase. 10 at. % potassium doping increases the conductivity of the compound by over 2 orders of magnitude to 450 S/cm, always forming the high temperature β-phase. Metallic type behavior is observed

in $Ba_{1-x}K_xCu_2S_2$ for x>0.005. The values of the Seebeck coefficient and their temperature dependence for $BaCu_2S_2$:K are typical for degenerate semiconductors.

$BaCu_2Se_2$ forms only one phase, similar to that of β-$BaCu_2S_2$. The K doping is found to enhance the transport properties even more than for the sulfide samples. The highest conductivity (740 S/cm) in p-type pressed powder pellets of $Ba_{0.9}K_{0.1}Cu_2Se_2$ is reported. $BaCu_2Se_2$ has an unusually high Seebeck coefficient in the undoped form and falls of rather sharply when doped by potassium. Although temperature dependent transport measurements are not available, the high conductivity and low Seebeck coefficient of the $BaCu_2Se_2$:K are likely to confirm the degenerate semiconducting nature of the samples.

Chapter 5. Conclusions and suggestions for further work.

In this work the structural, optical and transport properties of two material systems are presented and discussed. This includes systematic studies of the effect of substitutional and interstitial dopants on p-type conductors. The relevance of the study lies in the possibility of quite precise control of the doping level and determination of its influence on the properties of the materials.

Substitutional doping of $CuScO_2$ with Mg on the Sc sites to form $CuSc_{1-x}Mg_xO_2$ with $0<x<0.15$ shows improvement in the conductivity of pressed powder samples up to the apparent solubility limit of Mg at $x = 0.06$. As a result the conductivity of the can be modulated by about an order of magnitude up to $1.5 \cdot 10^{-2}$ S/cm, compared to $7 \cdot 10^{-4}$ S/cm of the undoped 3R polymorph of $CuScO_2$. A decrease along the *a*-lattice parameter axis is also observed with the introduction of the Mg dopant, presumably leading to a higher overlap of Cu *d*-band electron orbitals. Increment of Mg concentration above $x = 0.06$ leads to decreased conductivity, due to formation of scattering sites, and an observable Mg residue in the samples. The advantage of substitutional doping lies in the minor influence on the absorption spectrum of the powders, with an unchanged optical band gap of 3.3 eV. The still rather low conductivity and carrier mobility in $CuSc_{1-x}Mg_xO_2$ remains a disadvantage towards practical applications.

Oxygen intercalation of the $CuSc_{1-x}Mg_xO_2$ pressed pellets, leading to incorporation of oxygen atoms on interstitial sites in the Cu layer of the structure and an expansion along the *a*-axis, is shown to enhance the transport properties of the samples. Again the highest conductivity of 0.5 S/cm is observed in $CuSc_{0.95}Mg_{0.05}O_{2+y}$, which also shows the highest level of intercalated oxygen $y = 0.23$. It is not understood why the highest oxidation level occurs in the sample with $x = 0.05$, which has a lower *a*-lattice parameter than, for example, the sample with $x = 0.01$, in the simultaneous intercalation process. The formation of two distinct oxidation states of $CuScO_2$ and $CuScO_{2.5}$ is observed in the powders, regardless of the presence of Mg.

The improved conductivity of $CuSc_{1-x}Mg_xO_{2+y}$ is crucial for TCO applications, but the oxidation process is found to greatly affect the optical properties of $CuScO_2$ towards increased absorption in the visible spectrum. This can be attributed to presence

of a higher carrier concentration in the valence band and broader impurity band formation, which is the origin of improved transport properties.

Further studies on $CuScO_2$ with dopants other than Mg should be carried out, with ionic radii close to that of Sc, for example Cu, Ca, Ag, or maybe even by monovalent cations (Li). The possibility of n-type doping by tetravalent cations (Sn, Fe, Mn, Pd) would be also interesting. Synthesis of $CuScS_2$ could result in improved conductivity compared to the oxide, although also likely to decrease the optical band gap of the material.

Highly conductive p-type $BaCu_2S_2$ and $BaCu_2Se_2$ are also characterized. Both compounds exhibit improved transport properties upon potassium doping on the Ba site. A change from activated to metallic conduction mechanism is observed in $Ba_{1-x}K_xCu_2S_2$ with $x \geq 0.025$. The highest conductivity of 740 S/cm in $Ba_{0.9}K_{0.1}Cu_2S_2$ is approaching the order of magnitude of the commercially used n-type conductors as ZnO and ITO. A major drawback of this compound is its low band gap of 1.7 eV, which makes it inapplicable in transparent devices. Furthermore, S/Se based n-type materials have to be developed for practical applications.

Only the properties of α-$BaCu_2S_2$ in the thin film form are reported up to date. It is possible that the low temperature phase with potassium doping can be stabilized, leading to higher conductivity, and yet somewhat transparent thin films. Both, $BaCu_2S_2$ and $BaCu_2Se_2$, can be used in thin film structures not requiring transparency, but rather high conductivity and work function as solar cell contact material or iLED devices.

The study of $BaCu_2(S,Se)_2$ solid solutions can result in materials with high conductivity and Seebeck coefficient for thermoelectric applications.

Furthermore research of new materials for TC applications is in order. One of such materials is BaCuSF, with an optical band gap of 3.1 eV and an intrinsic conductivity of 0.15 S/cm in the thin film form. Better transport properties can be obtained by substitutional doping on the Ba site with K. A continuous band gap modulation can be achieved in BaCu(S, Se, Te)F solid solutions toward lower energies. It is also found to exhibit light emitting properties under UV irradiation.

References

1. R.L. Hoffman, et.al. J. Appl. Phys. **90** (2001) 5763
2. H. Yanagi et.al., Solid State Commun. **121** (2002) 15
3. K. Nomura et.al. Science, **300** (2003) 1269
4. H. Ohta et.al., Appl. Phys. Lett. **77** (2000) 475
5. F.A.Benko and F.P. Koffyburg, Phys. Chem. Solids, **45** (1983) 57
6. F.A. Benko and F.P. Koffyburg, Mat. Res. Bull., **21** (1986) 753
7. F.A. Benko and F.P. Koffyburg, Phys. Stat. Sol. (a), **94** (1986) 231
8. F.A. Benko and F.P. Koffyburg, Can. J. Phys., **63** (1985) 1306
9. H. Yanagi, S. Inoue, K. Ueda, H. Kawazoe, H. Hosono, and N. Hamada. J. Appl. Phys. **88** (2000) 4159-4163
10. H. Yanagi, T. Hase, S. Ibuki, K. Ueda, and H. Hosono, Appl. Phys. Lett. **78** (2001) 1583-1585
11. R. Nagarajan et al., (2001)
12. M.K. Jayaraj et al. (2001)
13. N. Duan, A. W. Sleight, M. K. Jayaraj, and J. Tate, Appl. Phys. Lett. **77** (2000) 1325-1326
14. H. Kim, J.S. Horvitz, A. Piqué, C.M. Gilmore, D.B. Chrisey. Appl. Phys. A, **69** (1999) S447
15. I.Hamberg and C.G. Granqvist. J. Appl. Phys. **60** (1986) R123
16. Cranciun V. et.al. Appl. Phys. Lett. **65** (1994) 2963
17. M.Chen, Z.L. Pei, X. Wang, C. Sun, L.S. Wen. J. Mater. Res. **16** (2001) 2118
18. Y. Yan, et.al. Phys. Rev. Lett. **86** (2000) 5723
19. Lee E.-C., et.al. Phys. Rev. B. **64** (2001) 085120
20. Wang L.G., A. Zunger (NREL). Phys. Rev. Lett. **90** (2003) 256401
21. T. Yamamoto, H.K. Yoshida. Jpn. J. Appl. Phys. **38** (1999) L166
22. Joseph M. et.al. Physica B v.**302-303** (2001) 140
23. Tsukazaki A., et.al. App. Phys. Lett. **81** (2002) 235
24. Sun X.W. et.al. J. Appl. Phys. **86** (1999) 408
25. Tang Z.K. et.al. Appl. Phys. Lett. **72** (1998) 3270

26. Jin B.J. et.al. Matt. Sci. Eng. **B71** (2000) 301
27. M.Lorenz, E.M. Kaidashev, et.al. Solid State Electronics. **47** (2003) 2205
28. Shuji Nakamura, Semiconductors and Semimetals, **48** (1997) 391
29. H. Morkoç, Nitride Semiconductors and Devices, Springer, 1999
30. F.M. Stefanka, et.al. Phys. Stat. Sol A, **194** (2002) 380
31. D.L. Young, J.F. Geisz and T.J. Coutts. APL 82 (2003) 1236
32. D. K. Shroder, *Semiconductor Material and Device Characterization*, 2e. Wiley-Interscience, New York, 1998, pp.2-14
33. N. E. Mott, Metal-Insulator Transition. Taylor & Francis, London 1990
34. F. J. DiSalvo. Science. **285** (1999) 703
35. Dara L. Easley, Senior Honors Thesis, OSU, 2003
36. G.W. Burns and M.G. Scroger. The calibration of thermocouples and thermocouple materials. Gaithersburg, MD: U.S. Dept. of Commerce, National Institute of Standards and Technology; 1989
37. K. Seeger. Semiconductor Physics: an introduction. Berlin; New York: Springer-Verlag, 1982
38. R.D. Barnard. Thermoelectricity in Metals and Alloys. Taylor & Francis, London 1972
39. N. E. Mott, Conduction in Non-Crystalline Materials. Oxford University Press, Oxford, 1993
40. G. Kortüm, Reflection Spectroscopy. Springer-Verlag New York Inc. 1969
41. R.W. Frei, J.D. MacNeil, Diffuse Reflectance spectroscopy in Environmental Problem-Solving. CRC-Press. 1973
42. Levi Kilcher, Senior Thesis. OSU, 2003
43. P.Kubelka and F.Munk, Zh. Tekh. Fiz. **12** (1931) 593
44. P.Kubelka, J.Opt.Soc.Am. **38** (1948) 448
45. J. Li, A. Yokochi, T. G. Amos, A. W. Sleight, Chem. Mater. **14** (2002) 2602-2606
46. R. J. Cava, W. F. Peck, Jr., J. J. Krajewski, S-W. Cheong, and H. Y. Hwang, J. Mater. Res. **9** (1994) 314-317
47. K. Isawa, Y. Yaegashi, S. Ogota, M. Nagano, S. Sudo, K. Yamada, and H. Yamauchi, Phys. Rev. B **57** (1998) 7950-7954

48. Y. Kakehi, S. Nakao, K. Satoh, T. Yotsuya, Thin Solid Films **445** (2003) 294-298
49. K. Ueda, T. Hase, H. Yanagi, H. Kawazoe, H. Hosono, H. Ohta, M. Orita, and M. Hirano, J. Appl. Phys. **89** (2001) 1790-1793
50. R. J. Cava, H. W. Zandbergen, A. P. Ramirez, H. Takagi, C. T. Chen, J. J. Krajewski, W. F. Peck, Jr., J. V. Waszczak, G. Meigs, R. S. Roth, and L. F. Schneemeyer, J. Solid State Chem. **104** (1993) 437-452
51. D. B. Rogers, R. D. Shannon, C. T. Prewitt, and J. L. Gilson, Inorg. Chem. **10** (1971) 723-727
52. L. F. Mattheiss, Phys. Rev. B, **R48** (1993) 18300-18303
53. J. Li, A. Yokochi, and A. W. Sleight, submitted to Chem. Mater., (2003).
54. H. Yanagi, S. Park, A. D. Draeseke, D. A. Keszler, and J. Tate, J. Solid State Chem. **175** (2003) 34-38
55. International Center for Diffraction Data, JCPDS 79-0599, 77-2496
56. Effective ionic radii from R.D. Shannon, Acta Crystallogr. Sect. A **32** (1976) 751-767
57. K. Hayashi and M. Kato, Nihon Kagaku Kaishi, (1979) 2241. In Japanese, no volume number
58. International Center for Diffraction Data, JCPDS 83-1256
59. B. Nielsen, M.S. thesis, Oregon State University, 2004
60. D. L. Easley, private communications
61. C.-H. Park, D.A. Keszler, H. Yanagi, J. Tate. Thin Solid Films. **445** (2003) 288
62. C.-H. Park, D.A. Keszler, unpublished
63. K. Ueda, S. Inoue, H. Hosono, N. Surukura, M.Hirano. Appl. Phys. Let. **78** (2001) 2333
64. H. Hiramatsu, K. Ueda, H. Ohta, M. Hirano, T. Kamiya, and H. Hosono. Appl. Phys. Lett. **82** (2003) 1048
65. H. Yanagi, J. Tate, S. Park, C.-H. Park, D. A. Keszler. Appl. Phys. Lett. **82** (2003) 2814
66. J.E. Iglesias, K.E. Pachali, H. Steinfink. J. Solid State Chem. **9** (1974) 6
67. M. Saeki, M. Onada, H. Nozaki. Mater. Res. Bull. **23** (1988) 603
68. X. Zhang, T. Hogan, C. R. Kannewurf, M. G. Kanatzidis. J. Alloys and Compounds. **236** (1996) 1

69. T. Ohtani, H. Takeuchi, K. Koh, T. Kaneko. J. Alloys and Compounds. **317-318** (2001) 201
70. Y.C. Wang and F. J. DiSalvo. J. Solid State Chem. **156** (2001) 44
71. S. Park, D. Keszler, M. M. Valencia, R. L. Hoffman, J. P. Bender, J. F. Wager. Appl. Phys. Lett. **80** (2002) 4393